

Forschungszentrum Jülich

**Kaon Pair Production in pp Collisions
at the ANKE Spectrometer**

Ph.D. Thesis Submitted to
the Physics Faculty of
Tbilisi State University
by

Irakli Keshelashvili

Jülich,
21 August 2006

Abstract

In the framework of this thesis the near-threshold production of ϕ mesons in the $pp \rightarrow pp\phi$ reaction has been studied at the Cooler Synchrotron COSY-Jülich, using the internal beam and ANKE facility. The physics motivation, the experimental setup, the data analysis procedures, the experimental results and their implications on the theoretical predictions are presented.

Meson production near threshold has the potential to clarify important questions of hadron physics in the non-perturbative regime of quantum chromodynamics due to its comparatively simple scheme of interpretation. The production of light vector mesons, $\rho(770)$, $\omega(782)$ and $\phi(1020)$, quark anti-quark states with their spins aligned ($J^P=1^-$) and without open strangeness, has been investigated with both hadronic and electromagnetic probes in order to study production mechanisms, coupling constants, modifications in nuclear medium and in particular the so-called Okubo-Zweig-Iizuka (OZI) rule.

This rule states that processes with disconnected quark lines between initial and final states are suppressed compared to those where the incident quarks continue through to the exit channel. As a result, the production of ideally mixed ϕ -mesons (quark content $s\bar{s}$) in a reaction $A + B \rightarrow \phi X$ is reduced compared to $A + B \rightarrow \omega X$ (ω is a linear combination of $u\bar{u} + d\bar{d}$) under similar kinematical conditions. Taking into account deviations from ideal mixing between singlet and octet vector mesons, Lipkin predicted a ratio of single ϕ to ω -production of $R_{\phi/\omega} = 4.2 \times 10^{-3} \equiv R_{\text{OZI}}$. However, strong enhancements of the experimental $R_{\phi/\omega}$ compared to R_{OZI} have been observed in particular in $\bar{p}p$ annihilations, where $R_{\phi/\omega}$ can be as large as $\sim 100 \times R_{\text{OZI}}$. Since vector-meson production in close-to-threshold $pp \rightarrow ppV$

reactions must proceed via the spin-triplet entrance channel, the investigation of the cross section ratio $\sigma(pp \rightarrow pp\phi)/\sigma(pp \rightarrow pp\omega)$ at small excess energies ε should provide a clean way of investigating possible violations of the OZI rule.

Total cross sections for ω -production in proton-proton collisions have been measured in a range of excess energy ε from a few MeV up to several GeV, whereas data for $pp\phi$ are very scarce. Two total cross sections of ϕ -production have been obtained for $\varepsilon \sim (2 - 4)$ GeV, but with rather limited accuracy. At low excess energy, a single measurement of total and differential cross sections has been made by the DISTO collaboration at $\varepsilon = 83$ MeV. In combination with the ω cross section of COSY-TOF at $\varepsilon = 92$ MeV, this yields $R_{\phi/\omega} \sim 7 \times R_{\text{OZI}}$. The differential distributions from DISTO indicate that ϕ -production at that energy proceeds dominantly via the 3P_1 (pp) entrance channel, though other partial waves do contribute significantly. To clarify this, it is crucial to extend the measurements to such small excess energies that only the lowest partial waves can contribute. Such measurements have become feasible at the internal proton beam of the Cooler Synchrotron COSY at the Research Center Jülich, using the ANKE target and detector facility. The $pp \rightarrow pp\phi$ reaction has been studied by detecting the K^+K^- decay of ϕ -mesons in coincidence with one of the forward-going protons.

In this thesis it is reported on the results for total cross section measurements of ϕ -production in proton-proton collisions at three beam momenta, corresponding to excess energies of $\varepsilon = 18.5, 34.5$ and 75.9 MeV, all of which are much closer to threshold than previous data. The lowest energy result demonstrates the dominance of the transition from the 3P_1 (pp)-entrance channel to the 1S_0 (pp) final-state. Both the total cross section and the proton-momentum spectrum indicate a significant pp final state interaction. Using data for ω -production from literature, it is found that $R_{\phi/\omega}$ is about $8 \times R_{\text{OZI}}$. The new data on the ω -production at ANKE, allow us to extract the OZI ratio with greater confidence and smaller error bars than before.

Contents

I	Introduction	1
1	Introduction and Motivation	3
1.1	General Physics Background	3
1.1.1	Quark Model	4
1.1.2	Hadronic Systems	5
1.1.3	Vector Mesons and Mixing	8
1.2	Okubo–Zweig–Iizuka (OZI) Rule	10
1.3	Test of the OZI–Rule	14
2	Background for the Measurement	17
2.1	Meson Production Near Threshold	17
2.1.1	Discussion/Introduction of a Simple Model	18
2.2	Physics Case for the Experiment	24
II	Experiment	25
3	Experimental Equipment: COSY and ANKE	27
3.1	Accelerator and Storage Ring COSY	27
3.2	ANKE Spectrometer and Detection Systems	28
3.2.1	Positive Side Detectors	29
3.2.2	Negative Side Detectors	32
3.2.3	Forward Detectors	34
3.3	Electronics and Data Acquisition	37
3.4	Experimental Settings for the Measurement	39
4	Data Analysis Procedures	41
4.1	Event Reconstruction	42

4.1.1	Tracking	42
4.1.2	Determination of Chamber Efficiencies	47
4.1.3	Momentum Reconstruction and Resolution	48
4.2	Trigger and Data Acquisition Efficiency	50
4.2.1	Data Taking Efficiency	52
4.3	Particle Identification	53
4.3.1	K^+ Selection	54
4.3.2	Time-Of-Flight Calibration and Selection	55
4.3.3	$K^+ K^-$ Correlation	57
4.3.4	Missing-Mass Selection	58
4.4	Result for the $pp \rightarrow pp\phi$ Reaction	58
5	Luminosity Determination	61
5.1	pp Elastic Scattering Cross-Section	62
5.2	Acceptance for pp Elastic Scattering	63
5.3	Selection of pp Elastic Scattering	64
5.4	Luminosity calculation and error estimation	67
5.5	Cross Check via Energy Loss Measurement	69
5.5.1	Measurement of the Target Thickness	69
5.5.2	Determination of η by a Measurement of the Com- paction Factor α	70
5.5.3	Measurement of the Ion Flux	71
5.6	Luminosity calculation and error estimation	72
5.7	Results	74
III	Physics Results	77
6	Results and Discussion	79
6.1	Acceptance Determination for $pp \rightarrow ppK^+K^-$	79
6.2	K^+K^- Invariant Mass Distributions	81
6.3	Cross-Sections	83
6.3.1	Total Cross-Sections	83
6.3.2	Differential Cross-Sections	85
6.4	OZI Result	87
6.5	Outlook	91
A	Properties of the ϕ Meson	93

Part I

Introduction

CHAPTER 1

INTRODUCTION AND MOTIVATION

In this chapter, the scientific background of the thesis – matter being composed of hadrons, which themselves are bound states of quarks – is introduced. In addition, the motivation for the specific experiment on which the thesis is based – test of the OZI-rule via ϕ (1020) meson production on proton-targets close to the production threshold will be outlined.

1.1 General Physics Background

Scientists have in the past discovered the different layers of compositeness of matter as we know them today: bulk matter is made of atoms (molecules), which themselves are build from an electron cloud and a nucleus, containing protons and neutrons. Protons, neutrons and electrons were originally thought to be “fundamental particles”, i.e. the building blocks of all the matter that we see around us in Nature. This still holds for the electron as of today. It soon turned out, however, that more and more particles were discovered, which appeared to be just as elementary as protons and neutrons. Therefore, the search of a further and deeper layer of substructure was started: the result – *quarks* – is known to every nuclear scientist, most

physicists, as well as many people with interest in the nuclear sciences.

1.1.1 *Quark Model*

The introduction of the quark model was driven by the idea of reducing the number of elementary particles after the proliferation of such objects, when more and more powerful accelerators became available in the 1950s. As early as 1949, C. N. Yang and E. Fermi speculated that the *pion* (π) was a nucleon–antinucleon composite [1]. After the discovery of strange particles, such ideas were taken on by others, most notably S. Sakata, who introduced the *lambda* (Λ) as the strange fundamental building block besides proton and neutron [2]. The contest between different competing models was finally resolved by the discovery of the *omega-minus* (Ω^-) at Brookhaven (BNL, USA), which was the missing member of one particular particle multiplet predicted by the SU(3)–model of M. Gell–Mann.

In the early 1960s M. Gell–Mann suggested that mesons and baryons be composed of entities which have become known as quarks (Gell–Mann is said to have taken this name from a phrase in James Joyce’s novel “Finnegan’s Wake”) [3]. It is interesting to note that such a model was proposed independently by G. Zweig, who called his constituents *aces* (but who never published his version in a refereed journal).

To cut a long story short: today, we believe that matter is composed of 6 different quarks, which were given the names:

$$\begin{array}{c|c|c} \mathbf{u} & \textit{up} & \mathbf{c} & \textit{charm} & \mathbf{t} & \textit{top} \\ \mathbf{d} & \textit{down} & \mathbf{s} & \textit{strange} & \mathbf{b} & \textit{bottom} \end{array}$$

One of the truly remarkable properties of quarks is that they have non-integral values of charges (in terms of the elementary charge e_0), i.e. $2/3$ (for u , c , and t), and $-1/3$ (for d , s , and b). (The signs reverse for the corresponding antiquarks.) In this way, the former elementary particles are

simple multiquark combinations, e.g.:

$$\begin{array}{lll} \text{Proton:} & p = uud & (\text{charge: } +1 = 2/3 + 2/3 - 1/3) \\ \text{Neutron:} & n = udd & (\text{charge: } 0 = 2/3 - 1/3 - 1/3) \\ \text{Lambda:} & \Lambda = uds & (\text{charge: } 0 = 2/3 - 1/3 - 1/3) \end{array}$$

(It must be noted here that this description ignores the virtual quark–antiquark pairs, which are present in hadrons (*sea-quarks*) – the quark-model as outlined above is thus a very simplified version, sometimes called the (naive) *constituent quark model*.)

The most important and possibly also astounding property of quarks is that they can never be found isolated, but only in (certain) bound states (see discussion below). This characteristic is called confinement in the underlying theory of the strong interaction (i.e. the interaction between quarks by the exchange of *gluons*), called *quantum chromodynamics* (QCD). Here, it suffices to mention that only two combinations of quarks have been unambiguously identified up to now: *baryons* (made of 3 quarks, examples: proton, neutron), and *mesons* (quark–antiquark states, example: pion) – other multiquark bound states are searched for vigorously and recently, evidence for *pentaquarks* (i.e. 5 quark-states) has been reported, but this needs to be confirmed.

For more details on the quark model as well as on QCD, we refer to the multitude of literature and textbooks on the subject.

1.1.2 Hadronic Systems

The early success of the quark-model was that it brought order into the “zoo of particles” of *hadrons*, i.e. baryons and mesons [4]. The following discussion uses only the three low-mass quarks (*u*, *d*, *s*), but it can be extended to the *c*-quark; for the *t*- and *b*-quarks, however, the underlying symmetry is too badly broken due to their large masses.

Table 1.1: Additive quantum numbers of the three lowest mass quarks and antiquarks. Here, Q is the electric charge in units of e_0 , I is the isospin, I_3 the third component of the isospin, Y is the hypercharge, S is the strangeness, and B is the baryon number. $Q = Y/2 + I_z$, $Y = B + S$.

Quark \ Property	Q	I	I_z	Y	S	B
u	$2/3$	$1/2$	$1/2$	$1/3$	0	$1/3$
d	$-1/3$	$1/2$	$-1/2$	$1/3$	0	$1/3$
s	$-1/3$	0	0	$-2/3$	-1	$1/3$
\bar{u}	$-2/3$	$1/2$	$-1/2$	$-1/3$	0	$-1/3$
\bar{d}	$1/3$	$1/2$	$1/2$	$-1/3$	0	$-1/3$
\bar{s}	$1/3$	0	0	$2/3$	1	$-1/3$

Using a group-theoretical approach to the hadronic symmetries and starting from the fundamental quark-triplet (Fig. 1.1), so-called multiplets of baryons and mesons are obtained, in which the order parameters are: (i) mass, (ii) charge and (iii) strangeness S (other choices are possible, see below). In Fig. 1.2, examples are given for the baryon-octet, containing proton

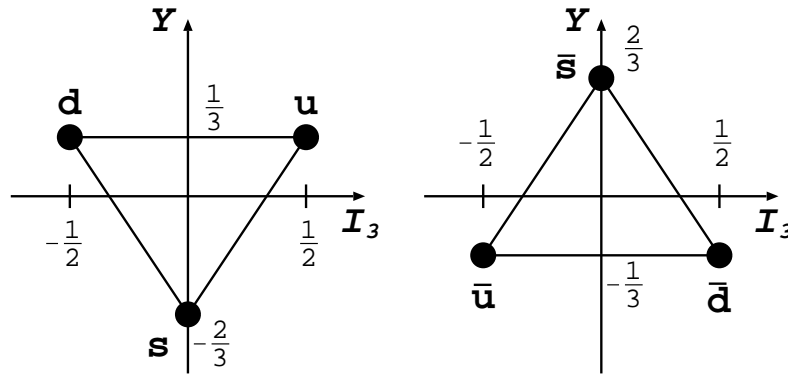


Figure 1.1: Fundamental triplets of (u, d, s) and $(\bar{u}, \bar{d}, \bar{s})$. Y is the hypercharge and I_3 the third component of the isospin (see also Table 1.1).

and neutron as well as the meson-nonet with the pion. In these figures, particles along horizontal lines have similar masses (exception: π, η), while vertically the mass of the hadron depends on the number of s -quarks as

compared to the lighter u - and d -quarks.

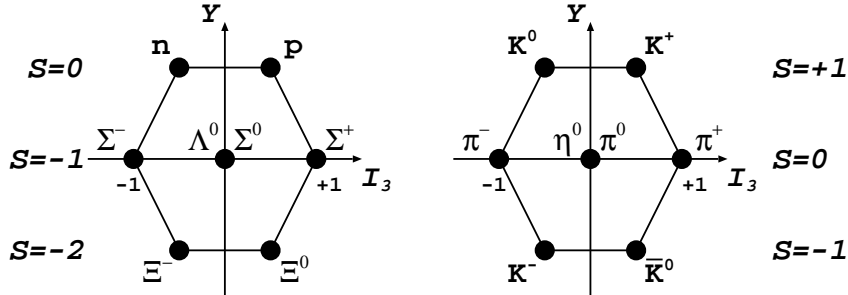


Figure 1.2: Baryon octet (left) and meson nonet (right).

For the further discussion we need to consider in more detail the mesons, the bound states of a quark and an antiquark: all such states are unstable and will decay sooner or later. Because of the *quantum numbers* of the quark-constituents and possible orbital angular momenta of the quarks in a meson, the resulting mesons can be divided into the following different categories:

- | | | |
|------|---------------------|-------------|
| I) | Pseudoscalar Mesons | $J^P = 0^-$ |
| II) | Vector Mesons | $J^P = 1^-$ |
| III) | Scalar Mesons | $J^P = 0^+$ |
| IV) | Tensor Mesons | $J^P = 2^+$ |

The pseudoscalar mesons have quark and antiquark spins antialigned and zero orbital angular momentum, resulting in a total angular momentum of zero. Since the parity of an antiquark is opposite to that of the quark, this leads to them having negative parity. Prominent members are the pions (π^- , π^0 , π^+).

The vector mesons have quark and antiquark spins aligned and zero orbital angular momentum, thus the total angular momentum is 1. They also have negative parity. Examples of vector mesons are *rho* (ρ), *omega* (ω), and *phi* (ϕ).

The scalar mesons have aligned spins and one unit of orbital angular momentum, and resulting in a total angular momentum of zero and positive

parity. Examples are a_0 and f_0 , although not undisputed.

Finally, the tensor mesons, have aligned spins, which, together with the orbital angular momentum adds up to a total angular momentum of two; they too have positive parity. Within our context the latter two (as well as many other mesons with higher orbital angular momentum) do not play a role and will not be discussed further. A trivial reason is that usually higher orbital angular momenta translate into a higher mass for the meson, and these are no longer experimentally accessible at COSY (see below).

1.1.3 Vector Mesons and Mixing

As noted above, the vector mesons ($J^P = 1^-$) can be understood as $l = 0$, spin-triplet quark–antiquark states. The nonet of vector mesons is shown in Fig. 1.3; in the following we concentrate on the non–strange members, i.e. rho (ρ^- , ρ^0 , ρ^+), omega (ω) and phi (ϕ).

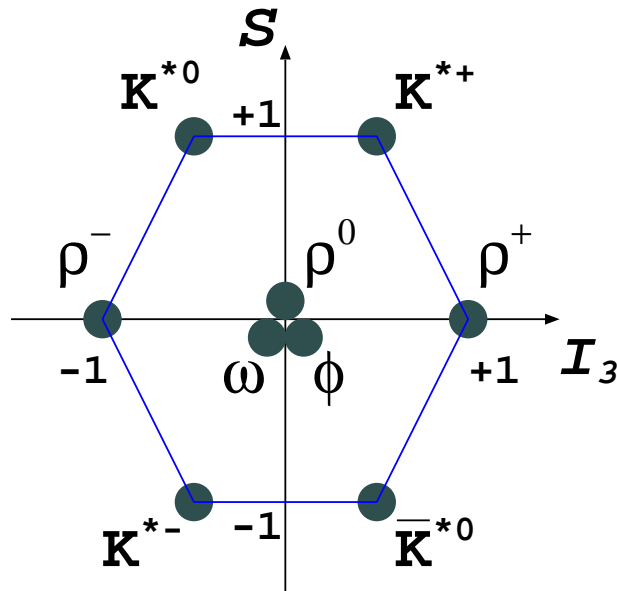


Figure 1.3: Nonet of vector–mesons.

The nonet can be understood as an octet and a singlet. Formally, one can write:

$$\phi = V_0 \sin \Theta - V_8 \cos \Theta$$

$$\omega = V_8 \sin \Theta + V_0 \cos \Theta$$

where ω and ϕ are the physical states, and V_0 , V_8 represent the singlet and the octet state, respectively. For ideal mixing, the mixing angle would be $\Theta_i \simeq 35^\circ$ ($\sin \Theta_i = \sqrt{1/3}$, $\cos \Theta = \sqrt{2/3}$), resulting in

$$\phi = \frac{1}{\sqrt{3}}(V_0 - \sqrt{2}V_8)$$

$$\omega = \frac{1}{\sqrt{3}}(V_8 + \sqrt{2}V_0)$$

where

$$V_0 = (\bar{u}u + \bar{d}d + \bar{s}s)/\sqrt{3}$$

$$V_8 = (\bar{u}u + \bar{d}d - 2\bar{s}s)/\sqrt{6}$$

thus yielding:

$$\rho^0 = (u\bar{u} - d\bar{d})/\sqrt{2}$$

$$\omega = (u\bar{u} + d\bar{d})/\sqrt{2}$$

$$\phi = s\bar{s}$$

This has the immediate consequence that the mass of the ρ^0 and of the ω should be very similar, while the ϕ -mass is significantly different (larger). The experimental masses are shown in Tab. 1.2. Since this is in line with

Table 1.2: Comparison of experimental masses for the ρ^0 , ω and ϕ mesons.

Particle	Mass	[MeV/c ²]
ρ^0	775.5	± 0.4
ω	782.65	± 0.12
ϕ	1019.46	± 0.019

the expectation for ideal mixing, it can be deduced that the experimental octet-singlet mixing angle is close to the ideal one. A detailed analysis yields $\Theta \approx 39^\circ$ (note: in the pseudoscalar meson case, the corresponding mixing angle is $\Theta \approx 11^\circ$).

As the bottom line of this discussion, it follows that the ω -meson has essentially only $u\bar{u}$ and $d\bar{d}$ components (and no strange quark part), while, on the contrary, the ϕ -meson practically only has an $s\bar{s}$ -component (i.e. very small $u\bar{u}$ and $d\bar{d}$ parts). This has immediate consequences for the corresponding meson-decays, which will be discussed in the following section.

1.2 Okubo–Zweig–Iizuka (OZI) Rule

Back in 1963, experimental evidence from experiments at Brookhaven indicated that the ϕ -meson predominantly decays into a kaon-antikaon pair rather than to a $(\rho + \pi)$ or 3π (see Fig. 1.4) as expected from the usual systematics of hadron decays [5]. G. Zweig interpreted this (see [7]) by assuming that the ϕ has hidden strangeness and visualized the decay as indicated in Fig. 1.5. The $\bar{s}s$ content of the ϕ persists through its decay and naturally leads to the final state mesons with strange-quark content rather than the non-strange ρ and π . The modern interpretation is that strong processes, in which the final state can only be reached through quark-antiquark annihilation (disconnected quark-lines in the above figures) are suppressed.

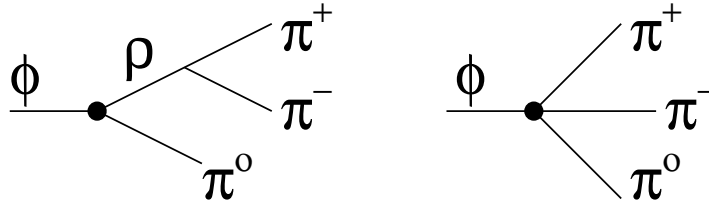


Figure 1.4: The diagram of $\phi \rightarrow \pi^+\pi^-\pi^0$ decay: via $\phi - \rho$ mixing (left); direct transition to 3π system (right).

In what has become known as the Okubo-Zweig-Iizuka (OZI) rule, one compares the production of ϕ - and ω -mesons under similar kinematical conditions. Since ω and ϕ have the same quantum numbers $I = 0$, $Y = 0$, one would expect that they should have very similar strong-interaction properties. In particular their strong decay width should be comparable. Experimentally this is not observed.

$$\begin{array}{rcl}
 \phi(1020) & \begin{array}{l} \rightarrow K^+K^- \\ \rightarrow K^0\bar{K}^0 \\ \rightarrow \pi^+\pi^-\pi^0 \end{array} & \left. \vphantom{\begin{array}{l} \rightarrow K^+K^- \\ \rightarrow K^0\bar{K}^0 \\ \rightarrow \pi^+\pi^-\pi^0 \end{array}} \right\} \begin{array}{l} 84\% \\ \\ 15\% \end{array} & \omega(783) & \begin{array}{l} \rightarrow \pi^+\pi^-\pi^0 \\ \rightarrow \pi^+\pi^- \\ \rightarrow \pi^0\gamma \end{array} & \left. \vphantom{\begin{array}{l} \rightarrow \pi^+\pi^-\pi^0 \\ \rightarrow \pi^+\pi^- \\ \rightarrow \pi^0\gamma \end{array}} \right\} \begin{array}{l} 90\% \\ \\ 10\% \end{array}
 \end{array}$$

The ω decays predominantly into the 3π channel, while for the ϕ this channel is suppressed relative to $\bar{K}K$ even though the phase space for the 3π channel is very small (m_ϕ is barely above $2m_K \simeq 996$ MeV). This indicates a strong preference for ϕ to decay into channels involving strange particles rather than into channels without strange particles.

Substituting the masses of the vector mesons, one obtains $\Theta=39^\circ$, which is not far from the ideal mixing angle. The difference $\delta = \Theta - \Theta_i$ is called deviation from the ideal mixing angle and determines the contribution of light quarks in the ϕ wave function. This contribution, according to the OZI rule, determines how large the cross sections of ϕ production are in NN , πN or $\bar{N}N$ interactions. To demonstrate this, let us write the formulation of

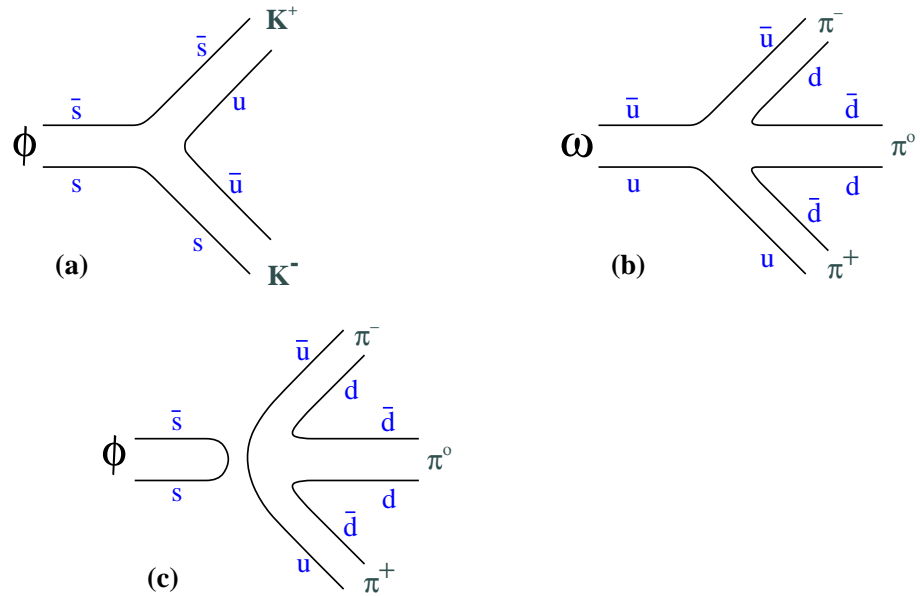


Figure 1.5: ϕ and ω decays: (a, b) allowed (or preferred) by the OZI rule; (c) Forbidden (or disallowed).

Okubo [29] in terms of mixing angles:

$$\frac{M(A + B \rightarrow C + \phi)}{M(A + B \rightarrow C + \omega)} = -\tan(\Theta - \Theta_i),$$

where $M(A + B \rightarrow C + q\bar{q})$ are amplitudes of the corresponding processes and

$$R = \frac{\sigma(A + B \rightarrow C + \phi)}{\sigma(A + B \rightarrow C + \omega)} = \tan^2 \delta \times f, \quad (1.1)$$

where f is the ratio of phase space of the reaction. If $f=1$ and $\Theta=39^\circ$ (the corresponding deviation from ideal mixing is $\delta \approx 3.7^\circ$) in Eq. 1.1, then the OZI rule predicts that in all hadron reactions the ratio between the cross sections of ϕ and ω production $R(\phi/\omega)$ should be [9, 10]:

$$R(\phi/\omega) = 4.2 \times 10^{-3} \equiv R_{OZI} \quad (1.2)$$

Therefore, using as input only the masses of mesons, the ratio of production cross sections is predicted .

It is remarkable to what extent the experimental data in different interactions and at different energies follow this rule. We will discuss this in detail in the next sections. The physical mixing angle could be calculated for each meson nonet using the quadratic Gell-Mann–Okubo mass formula. It means that the mixing is large and the production of the corresponding $\bar{s}s$ states will be suppressed in comparison with their light quark counterparts.

In QCD the Zweig-suppression is interpreted in terms of multi-gluon intermediate states: it is as well observed in charmonium-decays into non-charmed and charmed final states.

In the next section, it is discussed how the OZI-rule can be tested experimentally and which results have been obtained up to now.

1.3 Test of the OZI-Rule

Generally speaking, the OZI-rule can be tested by a comparison of the cross sections for ϕ -production compared to ω -production in the same reaction, for example πN , NN , $\bar{N}N$.

The production of the ϕ and ω mesons was studied in different experiments in NN , πN , and $\bar{N}N$ interactions. The obtained ratios $R(\phi X/\omega X)$ of the cross sections of ϕ and ω production are shown in Table 1.3 [12].

$$\frac{\sigma(\pi N \rightarrow \phi X)}{\sigma(\pi N \rightarrow \omega X)} = (3.2 \pm 0.8) \times R_{OZI} \quad (1.3)$$

Therefore, in πN interaction [11] the agreement with the OZI-rule prediction Eq. 1.2 is reasonable.

In contrast the weighted average ratio of the cross sections of the ϕ and ω production (from literature) at different energies in nucleon–nucleon interactions exceeds the OZI value of Eq. 1.2 by approximately three times:

$$\frac{\sigma(NN \rightarrow \phi X)}{\sigma(NN \rightarrow \omega X)} = (3.05 \pm 0.7) \times R_{OZI} \quad (1.4)$$

However, strong enhancements of the experimental $R_{\phi/\omega}$ compared to R_{OZI} have been observed (an overview is given in Ref. [12]), in particular, in $\bar{p}p$ annihilations, where $R_{\phi/\omega}$ can be as large [13].

$$\frac{\sigma(\bar{p}p \rightarrow \phi X)}{\sigma(\bar{p}p \rightarrow \omega X)} = \sim 100 \times R_{OZI} \quad (1.5)$$

i.e. more than a factor three.

The deviation from the OZI-rule prediction in the NN and $\bar{N}N$ scattering thus is significantly higher than in the πN interaction and deserves further investigations and will be treated in this thesis.

Next a brief introduction into meson production in NN collision would be given.

Table 1.3: The ratio $R = \phi X/\omega X$ of the cross sections for production of ϕ and ω mesons in $pp, \bar{p}p$, and πp interactions. P_L is the momentum of the incoming particle. No corrections on the phase space volume difference were made except the cases marked *.

Initial state	P_L [GeV/c]	Final state X	$R = \phi X/\omega X$ $\times 10^{-3}$
$\pi^+ n$	1.54–2.6	p	21.0 ± 11.0
$\pi^+ p$	3.54	$\pi^+ p$	19.0 ± 11.0
$\pi^- p$	5–6	n	3.5 ± 1.0
$\pi^- p$	6	n	3.2 ± 0.4
$\pi^- p$	10	$\pi^- n$	6.0 ± 3.0
$\pi^- p$	19	$2\pi^- \pi^+ p$	5.0^{+5}_{-2}
$\pi^- p$	32.5	n	2.9 ± 0.9
$\pi^- p$	360	X	14.0 ± 6.0
pp	10	pp	20.0 ± 5.0
pp	24	pp	26.5 ± 18.8
pp	24	$\pi^+ \pi^- pp$	1.2 ± 0.8
pp	24	$pp \ m\pi^+ \pi^-$, $m = 0, 1, 2$	19.0 ± 7.0
pp	70	pX'	16.4 ± 0.4
pp	360	X	4.0 ± 5.0
$\bar{p}p$	0.7	$\pi^+ \pi^-$	$19.0 \pm 5^*$
$\bar{p}p$	0.7	ρ^0	$13.0 \pm 4^*$
$\bar{p}p$	1.2	$\pi^+ \pi^-$	$11.0 \pm 5^{+3}_{-4}$
$\bar{p}p$	2.3	$\pi^+ \pi^-$	17.5 ± 3.4
$\bar{p}p$	3.6	$\pi^+ \pi^-$	$9.0 \pm 9^{+4}_{-7}$

CHAPTER 2

BACKGROUND FOR THE MEASUREMENT

Results on the near-threshold production of mesons in nucleon-nucleon scattering are very important because they are sensitive to the interactions of neutrons and protons at short distances. The analysis of such data in the short-range limit permits a quantitative comparison of the production leading to two- and three-body final states. The relative strengths of different meson productions are broadly in line with the predictions of one-meson-exchange models and it is deviations from these that may be indications of extra physics. In this chapter we will discuss the results from one of such simple model, which was presented by Colin Wilkin at the Baryon '98 Conference in Bonn [14].

2.1 Meson Production Near Threshold

Meson production analysis near threshold should be considered only as a zeroth order approach to the understanding of these processes. However, it may at least indicate the sensitivity of the results to the physics assumptions,

and therefore what one might hope to learn from more refined models.

2.1.1 Discussion/Introduction of a Simple Model

Most analyses of the $NN \rightarrow NN X$ reaction have been carried out in one-boson-exchange models, shown schematically in Fig. 2.1, which serves to define the kinematics in the overall c.m. system. Letting \vec{k} be the meson momentum, and $2\vec{q}$ the relative NN momentum in the final state, then non-relativistically the c.m. kinetic energy ε of the $NN X$ system is

$$\varepsilon = \frac{1}{2\mu_R} k^2 + \frac{1}{m} q^2. \quad (2.1)$$

Here m is twice the nucleon reduced mass, μ the meson mass and μ_R the overall reduced mass equal to $\mu/(1 + \mu/2m)$. Data are often presented in terms of η , the maximum c.m. momentum of the meson in units of the meson mass

$$\eta = \sqrt{2\mu_R\varepsilon}/\mu. \quad (2.2)$$

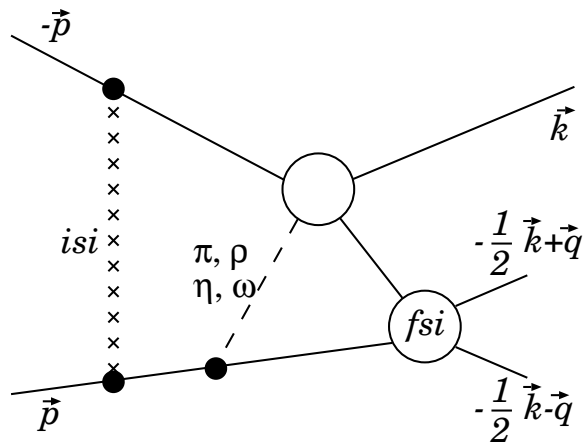


Figure 2.1: One-boson-exchange mechanism for meson production

Calculations differ according to what mesons X are exchanged in the diagram, whether distortion of the incident NN waves or rescattering of the meson X are included. However, what is crucial in any description is a reasonable treatment of the nucleon-nucleon final-state interaction (FSI), drawn here as a blob. This is because of the nearby poles in the S -wave NN amplitudes at $q^2 = -\alpha^2$, corresponding to the deuteron bound state in the 3S_1 channel or in the 1S_0 virtual state. Taken together with the phase space factors, these poles tend to determine much of the energy dependence of the total cross section for meson production. Furthermore, in any region where these poles dominate, it is possible to link quantitatively meson production in cases where the two nucleons emerge separately or as a bound deuteron state.

The production of a pion or heavier meson in nucleon–nucleon scattering necessarily involves very large momentum transfers and so it is primarily the short–range part of the production operator which is tested in such processes. However, it is precisely at short distances that the extrapolation theorem allows us to approximate the scattering wave function in terms of that for the bound state. As a consequence, independent of the details of the operators, the production amplitudes \mathcal{M} are linked by

$$\mathcal{M}(NN \rightarrow \{NN\}_q X) \approx -\mathcal{M}(NN \rightarrow \{NN\}_{bs} X) / \sqrt{2\alpha(q^2 + \alpha^2)}. \quad (2.3)$$

The above relation is of course only valid for S -wave spin-triplet NN final states, where the bound state is the deuteron. However, the wave function for the virtual state in the spin-singlet system with $\alpha < 0$ has an energy dependence dominated by a similar $1/\sqrt{q^2 + \alpha^2}$ factor to the bound state case of Eq. (2.3). The main difference between the two cases is that there is then no equivalent of the deuteron channel to normalize the cross section.

The cleanest place to test such an approach is in the comparison of the cross sections for $pp \rightarrow pn\pi^+$ and $pp \rightarrow d\pi^+$ away from threshold but in those parts of phase space where the np excitation energy $\varepsilon_{pn} = q^2/m$ re-

mains small. Under these conditions we expect that the final S -wave triplet contribution to the differential cross section should be

$$\frac{d^2\sigma}{d\Omega dx}(pp \rightarrow \{np\}\pi^+) \approx \frac{k(x)}{k(-1)} \frac{\sqrt{x}}{2\pi(x+1)} \frac{d\sigma}{d\Omega}(pp \rightarrow d\pi^+). \quad (2.4)$$

The dimensionless variable x is defined as $x = \varepsilon_{pn}/E_B = q^2/mE_B$, where E_B is the deuteron binding energy, and $k(x)$ and $k(-1)$ are the momenta of the pion in the three and two-body reactions respectively. Very detailed measurements of pion production were carried out by a TRIUMF group [15] and the results were consistent with the expectations based on the above formulae.

Applying the formalism to near-threshold production, the condition on ε_{np} is always met. If the energy dependence of the two-body cross section is of the form

$$\sigma_T(pp \rightarrow d\pi^+) = A\eta + B\eta^3, \quad (2.5)$$

the integrals over phase space can be performed analytically [16] to give

$$\begin{aligned} \sigma_T(pp \rightarrow pn\pi^+) \approx & \frac{1}{4}\zeta^3\eta^4 \left(1 + \sqrt{1 + \zeta^2\eta^2}\right)^{-2} \times \\ & \left\{ A + \frac{1}{2}B\eta^2 \left[1 + \frac{1}{2}\eta^2\zeta^2 \left(1 + \sqrt{1 + \zeta^2\eta^2}\right)^{-2}\right] \right\}. \end{aligned}$$

The only dependence upon the deuteron properties is through the parameter $\zeta = \mu_R/\sqrt{2\mu E_B}$. It should be mentioned that the approach has to be modified slightly to take into account, in an approximate way, external Coulomb corrections which are very important near threshold [17].

Turning now to proton-proton scattering, the short-range approximation

to the pion-exchange diagram of Fig. 2.1 predicts a total cross section of [19]

$$\sigma_T(pp \rightarrow ppX) = C \frac{(m + \mu)^2}{(2m + \mu)^{5/2}} \frac{\sqrt{\mu}}{(m\mu + m_\pi^2)^2} \times |f(\pi^0 p \rightarrow p X)|^2 \left(\frac{\varepsilon}{1 + \sqrt{1 + \varepsilon/E_B}} \right)^2 \quad (2.6)$$

where, including Coulomb distortion, $E_B \approx 0.45$ MeV. In addition to the amplitude $f(\pi^0 p \rightarrow p X)$ for the production of meson X in pion scattering, one also recognizes the last term here as being the S -wave FSI factor of Eq. (2.6). The normalization constant C is close to that required to reproduce the η -production data [18], but if these data are rather used to determine the value of C , then this has to be multiplied by factors of 1.3 and 3 in order to describe well the ω and η' data in Fig. 2.2. It is therefore clear that there are no gross departures from the most naive implementation of a one-pion-exchange model. We are therefore going to have to look in much greater detail and at more exclusive observables in order to see features which are dependent upon the particular meson produced. It should be noted, that the new ANKE measurements for ϕ -production at 3 excess energies (18.5 MeV, 34.5 MeV and 75.9 MeV) are included in this figure. How these data have obtained, which is the central part of the this thesis, will be discussed in the remaining chapter of this thesis.

Simple isospin arguments, combined with the values of the S -wave NN wave functions at short distances, suggest that the production of isoscalar mesons through one-pion exchange should be about four times higher in pn collisions than pp , and the recent TSL measurement of $pn \rightarrow pn\eta$ shows a cross section with a similar energy dependence to that of $pp \rightarrow pp\eta$ but a factor of 6.5 times stronger [24]. This implies that some other exchange is also very important. This could be the ρ meson, since the photon has a significant coupling to the $N^*(1535)$ isobar. Denoting by t_π the amplitude for π exchange, and similarly for ρ , η and ω , the TSL data are consistent

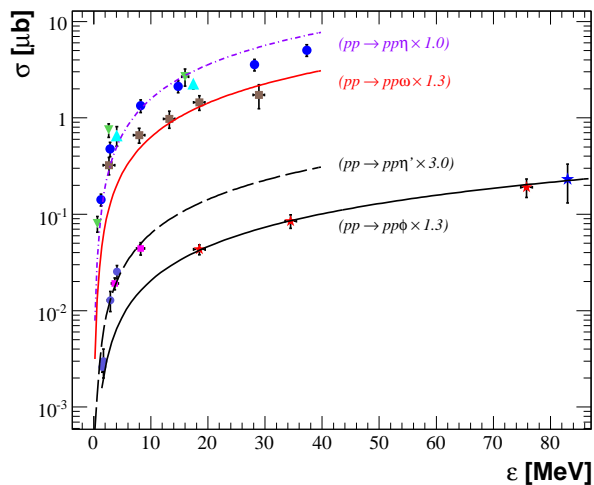


Figure 2.2: Total cross sections for meson production in the $pp \rightarrow ppX$ reaction near threshold. Experimental data on the production of η [19, 21, 22], ω [20], and η' -mesons [19, 23] are compared with the predictions of Eq. (2.6) normalized to the η data. The residual scale factors shown are close to unity except in the η' case. The only previously existing data on ϕ production is at $\varepsilon = 83$ MeV [30] and, whereas this is much too high for the S -wave assumptions to be valid, it is amusing that the curve shown for the ϕ does pass through this point. With red stars the new ANKE measurements are included.

with [24]

$$\frac{|t_\pi - t_\rho + (t_\omega - t_\eta)/3|}{|t_\pi + t_\rho + t_\omega + t_\eta|} \approx 1.3, \quad (2.7)$$

where the minus signs in the numerator arise from a combination of spin and isospin coupling.

Even if one neglects η and ω exchange, there are still solutions where the ρ dominates and others where it is the pion, and extra experimental data, such as angular distributions, are required. Vector-meson-dominance models suggest strongly that ρ exchange is the most important term in η production in proton-proton collisions near threshold. The destructive interference

between ρ and π exchange in the pp case should produce more η at 90° than at 0° but we expect the angular distribution in $pn \rightarrow d\eta$ to be flatter.

When applying the formula of Eq. (2.6) to vector meson production, there is an uncertainty of a factor of $3/2$ due to the ambiguity in the spin coupling but by far the biggest modification arises from the finite width of the meson which means that even at a nominal $\varepsilon = 0$ there is sufficient energy to produce the bottom half of the meson. After this effect is included, the energy dependence of ω production is well reproduced, apart possibly from the lowest point.

Comparison of ω and ϕ production is interesting because of the interpretation of the ratio in terms of (ω, ϕ) mixing and the OZI rule. The lowest energy at which $pp \rightarrow pp\phi$ had previously been measured corresponds to $\varepsilon \approx 82$ MeV [30], and this is far too high an energy for the S -wave assumptions used in Eq. (2.7) to be valid. Nevertheless it is amusing that the ϕ prediction shown in fig. 6 does in fact pass through the experimental value. However one can only pass judgment on the validity of the OZI rule in the $pp \rightarrow pp\phi/pp \rightarrow pp\omega$ ratio when more extensive data sets are available and when one has dynamical models for both reactions, *i.e.* one needs calculations and not merely “understanding”. A model of this kind, which has been produced by the Jülich group for the ω [25], is now being extended for the ϕ [26].

It is of course vital to be able to describe the production of vector mesons in nucleon–nucleon collisions since there are hopes that the study of these mesons in a nuclear medium, possibly excited through heavy-ion experiments, might shed light on the quark-gluon plasma or the restoration of chiral symmetry. In particular it is important to know whether their production in proton–neutron collisions is much stronger than in proton–proton. To resolve this question, it is hoped to carry out measurements of quasi-free $pn \rightarrow d\omega(\phi)$ at the COSY accelerator and such results are already available for ω production [27] and ϕ production [28]. These results from the ANKE

measurements will be discussed in last chapter. To go further one will then need data on angular distributions and spin observables and so there is more work for the years to come.

2.2 *Physics Case for the Experiment*

As discussed in Sec. 1.3, strong deviations from the OZI-expectation have been found in various reactions (sometimes this is called “OZI-violation” or “violation of the OZI-rule”). It is thus important to further test this rule in reactions close to the production thresholds, since then the dynamics is simple: e.g. there are no further complications due to higher partial waves.

At COSY-Jülich, such an investigation can be performed in *proton-proton* and *proton-neutron* collisions; in fact, ω -production in $pp \rightarrow ppX$ (X ... unobserved missing particle) has recently been studied by the TOF-collaboration [32], and thus a test of the OZI-rule needs the corresponding measurement for $pp \rightarrow pp\phi$.

With the ANKE spectrometer and its detection system, the reaction has been investigated at three excess energies above the production threshold via:

$$pp \rightarrow pp\phi \rightarrow ppK^+K^-$$

where the ϕ meson can be identified from the K^+K^- invariant mass. technique based on missing mass spectra of one undetected proton, calculated using the detected proton and the kaon pair.

In the remainder of this thesis the experiment, analysis and the results of the measurement at ANKE will be discussed. The results, which are the efforts of a large collaboration, have been published in **Physical Review Letters** [**Phys. Rev. Lett.** **96**, 242301 (2006)].

Part II

Experiment

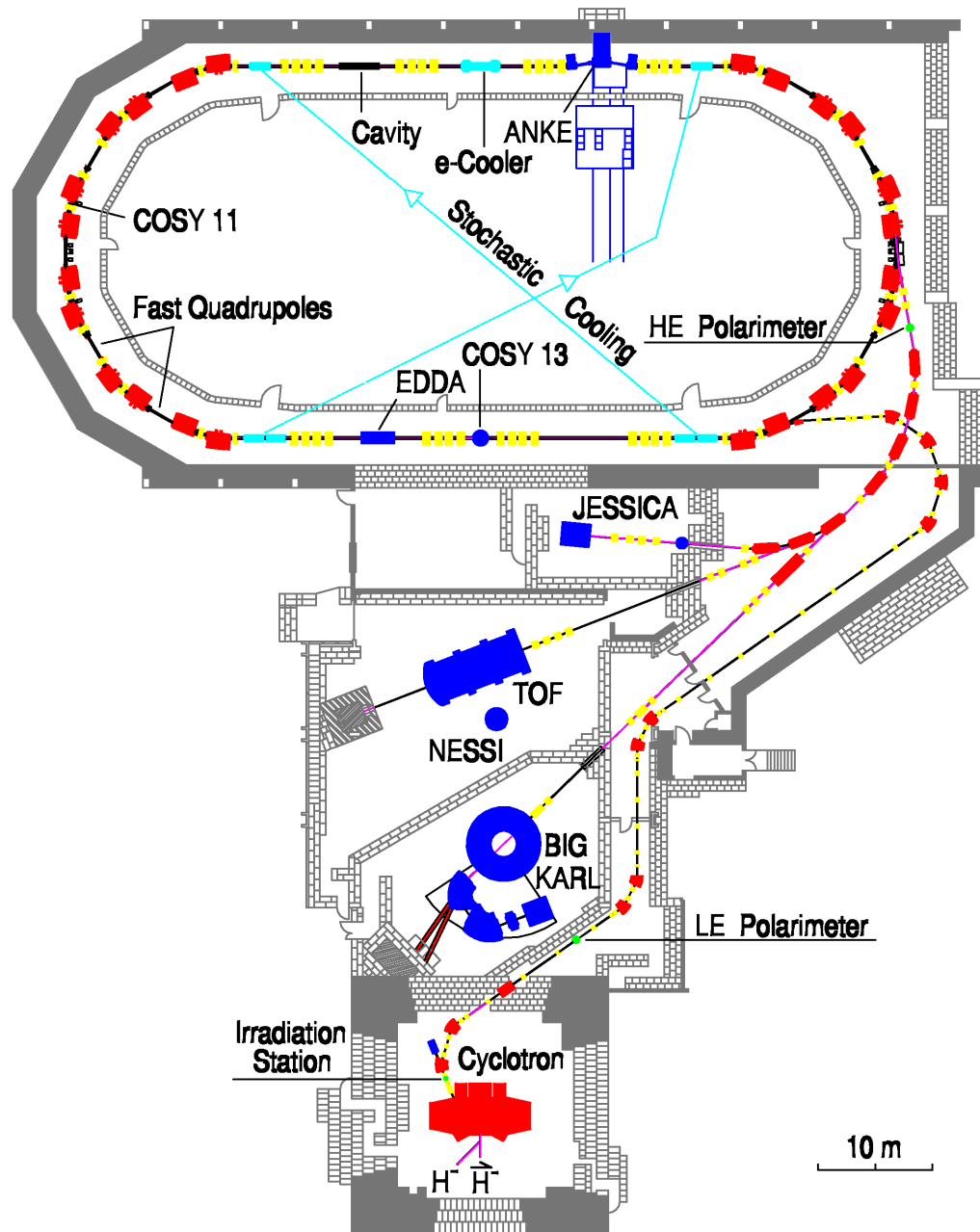


Figure 2.3: Layout of experiments at cooler synchrotron COSY. H^- and D^- ions are preaccelerated in the cyclotron JULIC and injected into the storage ring. In this sketch, four internal and five external experiments are also shown.

CHAPTER 3

EXPERIMENTAL EQUIPMENT: COSY AND ANKE

The experiment $pp \rightarrow pp\phi$ has been performed at the internal beam of COSY-Jülich, using the ANKE facility and a hydrogen cluster-jet target.

3.1 Accelerator and Storage Ring COSY

The accelerator and storage ring **COSY** ("COoler SYnchrotron") [33] at the *Forschungszentrum Jülich* can provide high quality polarized and unpolarized, proton (H^-) and deuteron (D^-) beams (Fig. 2.3, Page. 26). H^- and D^- ions are preaccelerated in the cyclotron JULIC and injected into the storage ring via a charge exchanging stripper carbon foil. This machine covers the momentum range from 295 MeV/c up to 3.65 GeV/c, corresponding to an energy range between 45 MeV and 2.83 GeV for protons, and from 67 MeV to 2.23 GeV for deuterons. COSY provides ion beams with momentum a resolution of $\Delta p/p = 10^{-3} - 10^{-4}$ and delivers up to 6×10^{10} protons in the ring (space charge limit is $\approx 2 \times 10^{11}$ p 's). The total length of the storage ring is 184 m. Electron cooling is applied up to 645 MeV/c. Also a stochastically

cooled beam can be provided in order to achieve the highest phase space density and to compensate beam deterioration due to beam-target interactions. This can be applied in the momentum range from 1.5 to 3.3 GeV/c. Beams can also be extracted and used at external target positions, but this is not of importance for the current discussion.

3.2 ANKE Spectrometer and Detection Systems

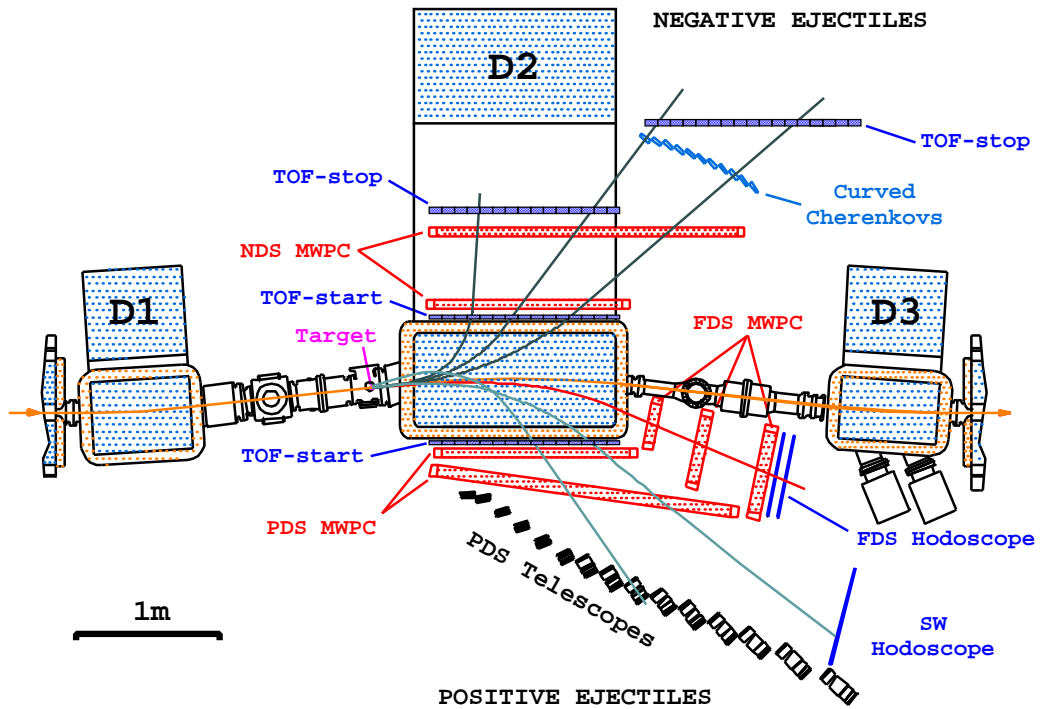


Figure 3.1: Sketch of the ANKE spectrometer and its detection systems. The color lines from target indicates tracks of scattered particles.

The "Apparatus for Studies of Nucleon and Kaon Ejectiles" (ANKE) [34] is one of the internal experiments situated in a straight section of the

COSY ring, as shown in Fig. 3.1. The ANKE Spectrometer consists of three dipole magnets, the identical dipoles D1 and D3 and a main dipole magnet D2. D1 deflects the circulating COSY beam by an angle α off its straight path onto a target which is placed in front of the D2. D2 is used as the spectrometer magnet for forward emitted ejectiles with beam deflection angle $-2\cdot\alpha$. D3 is used to guide beam back to the ring orbit. The D2 magnet is a rectangular C-type magnet with outer pole dimensions of 1400×658 mm². The pole edges are canted with 45° and 60° phases yielding a pole face area of 1240×460 mm² and a gap height of 200 mm. The deflection angle α can be adjusted to optimize the magnetic field independent of the beam momentum¹. At ANKE, various targets such as a cluster jet [35] or strip target can be used. Moreover, a Polarized Internal Target (PIT) has been constructed for measurements with polarized hydrogen and deuterium targets, which is currently commissioned.

The detector systems at the ANKE spectrometer can detect positively as well as negatively charged ejectiles. Thus, the reaction $pp \rightarrow pp\phi$ can be studied by detecting the K^+K^- decay of ϕ -mesons in coincidence with one of the forward-going protons, requiring that the three-particle missing mass (K^+K^-p) is consistent with the non-observed second proton. In the next sections the three main ANKE detector systems for the K^+ , K^- and proton identification are described.

3.2.1 Positive Side Detectors

The detector system for forward emitted low momentum positively charged particles can cover the momentum range of 150—1100 MeV/c. The general layout of positive detector system (PDS) is shown in Fig. 3.1. The START and STOP counters consist of vertically oriented plastic scintillators. The particles detected in this system pass one of the 23 time-of-flight (TOF)

¹within certain ranges

START scintillation counters behind the side exit window of D2 with a horizontal exit angle of $\pm 12^\circ$ and a vertical angle of $\pm 3.5^\circ$. After passing a two

Table 3.1: Dimensions of positive START scintillator

counter number	height [mm]	width [mm]	thickness [mm]
1-2	270	50	0.5
3-5	270	50	1.0
5-23	270	50	2.0

multi-wire proportional chamber (MWPC) for track reconstruction, particles are focused onto one of the 15 range telescopes or hit one of the 6 sidewall scintillation counters. Both chambers have been built at the *Forschungszentrum Rossendorf*, Germany. The sensitive areas are 350×1300 and 600×1960 mm², respectively. Both consist of three planes of anode wires (vertical, $+30^\circ$, and

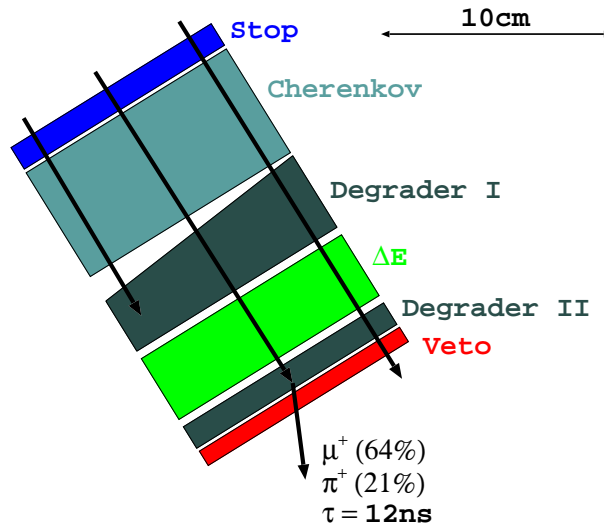


Figure 3.2: Sketch of the ANKE side telescope. It is composed of a STOP, a Cherenkov (only in telescope numbers 7 to 15), two degraders, and ΔE and veto scintillators.

-30°). The tungsten wires have a thickness of 20 and 25 μm in the smaller and larger chamber, respectively. The spacing between wires is 2.54 mm.

The cathodes are made of carbon and aluminum covered mylar foils with a thickness of about $20 \mu\text{m}$. The distance between the cathode and anode planes is 5 mm.

The range telescopes are placed in the focal plane of D2, each covering a momentum interval of roughly $30 \text{ MeV}/c$. The most useful information to distinguish particles in the PDS is the TOF between the START and STOP counters. The STOP scintillator counter is first part of a more complicated counter system called telescopes, shown in Fig. 3.2. The next part of telescope is a plastic Cherenkov counter in order to identify pions via light emission above a momentum of $300 \text{ MeV}/c$, which are used in telescopes 7 to 15 only. Behind the Cherenkov counters is a degrader made of copper, which stops protons from the target and decelerates kaons so that they just pass the following ΔE counter and are stopped in the second degrader. For the START counters, 1 inch phototubes (XP 2972) are used and 2 inch tubes (XP 2020) for the STOP detectors.

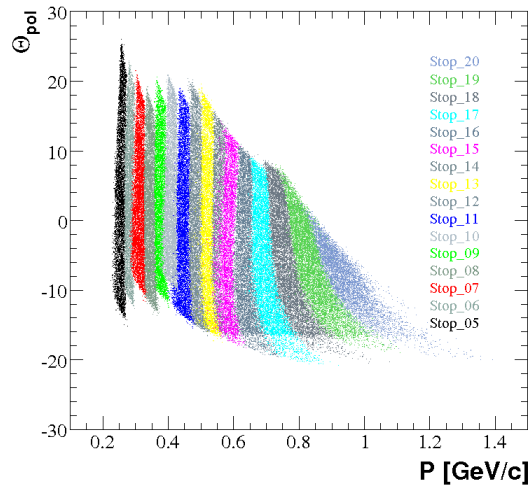


Figure 3.3: The angular *vs* momentum acceptance of the PDS. Different colors shows different STOP counters. With this distributions one can demonstrate that the telescopes are aligned along the focal plane.

For forward emitted high momentum particles which do not fall in the forward detector acceptance, the side hodoscope (so called Side Wall, SW) is installed in addition, as shown in Fig. 3.1. The SW consists of six vertically aligned scintillators and is used for a ΔE measurement as well as forward tracking. They are not aligned along the focal plane.

3.2.2 Negative Side Detectors

The negative-particle detection system (**NDS**) is placed inside the return yoke of the C-shaped D2 dipole magnet and partly outside the magnet in the forward direction (Fig. 3.1), where magnetic stray fields of D2 up to ≈ 200 mT are present. It consists of 20 vertically aligned START and 22 STOP (10 of

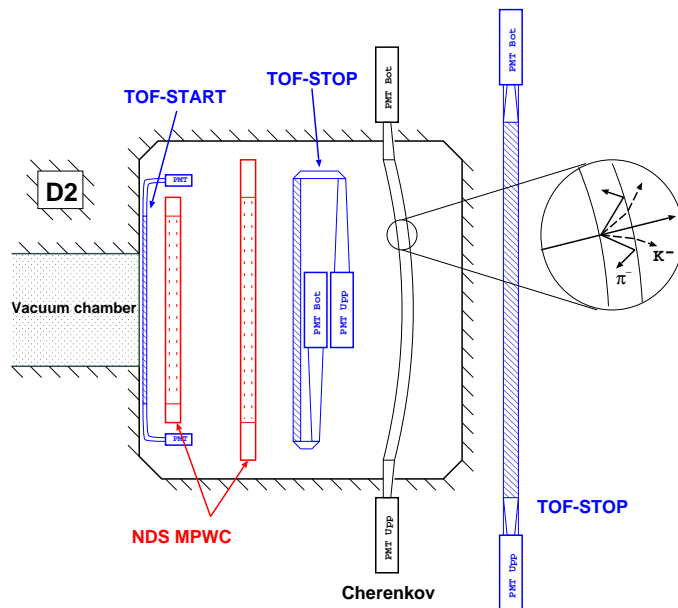


Figure 3.4: Sketch of side view of the NDS, most of which are inside the D2 return yoke.

them outside the dipole), and scintillator counters, used for particle identification via time-of-flight and ΔE -measurement. All START and STOP

counters are equipped with PMTs XP 2972 (23 mm diameter) and XP 2020 (44 mm diameter) respectively. Inside the D2 dipole magnet two multi-wire

Table 3.2: Dimensions of negative scintillator

counter number	height [mm]	width [mm]	thickness [mm]
START	270	50	2
STOP (1-12)	350	80	10
STOP (12-22)	250	150	20

chambers for track reconstruction are placed, with the same construction as for the PDS, which enable momentum determination with $\Delta p/p \approx 2\text{-}3\%$. In the forward direction, between START and STOP scintillator counters, 11 curved Cherenkov counters are installed for pion-kaon separation at high momentum. At the maximum field strength of D2 (≈ 1.6 T), negatively charged ejectiles can be measured in the momentum range from ≈ 120 to ≈ 1000 MeV/c. The horizontal and vertical angular acceptances are roughly $\alpha_{hor} = \pm 12^\circ$, $\alpha_{ver} = \pm 8^\circ$ at 200 MeV/c and $\alpha_{hor} = -2^\circ$ to 12° , $\alpha_{ver} = \pm 5^\circ$ at 1000 MeV/c. In the high momentum range of negative ejectiles the focal surface is far off, and thus the use of degraders is impossible. The time-of-flight difference between pions and kaons from START to STOP counters in the high momentum region is around 550 ps. The time resolution between START and STOP counters is similar and therefore not sufficient to separate high momentum kaons from the pion background. To provide sufficient separation power between pions and kaons, the time-of-flight information between the target and STOP-scintillator is used. In practice, the TOF between target and STOP counters is calculated by the measurement of the time difference of correlated K^+ and K^- . In this case the K^+ is detected in the PDS where the STOP counters are located in focal plane of spectrometer magnet and thus, particles passing certain START-STOP combination, have a well defined velocity β . The main advantage of this technique is the better time resolution of the thick STOP counters in comparison to the thin

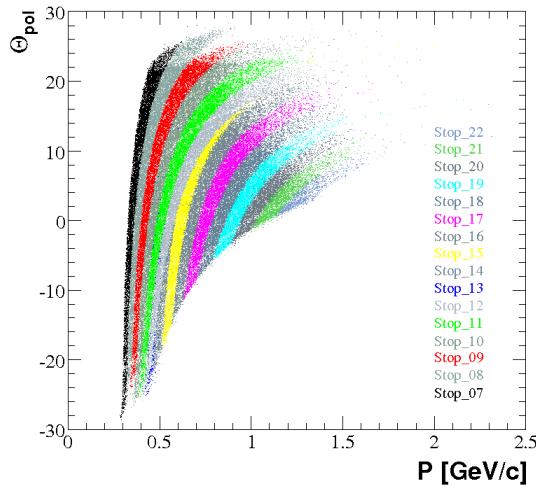


Figure 3.5: The angular *vs* momentum acceptance of the NDS. Different colors indicate different STOP counters.

START counters and moreover the longer path length from the target to the STOP counters, which leads to a larger time difference between pions and kaons. This technique will be discussed in more detail in Sec. 4.3.

3.2.3 Forward Detectors

The ANKE forward detector system (**FDS**) is located between the spectrometer dipoles **D2** and **D3** close to the beam pipe. The forward detector system consists of three multi-wire proportional chambers (FDS MWPC 1, 2, 3) and two layers of scintillation hodoscopes [36, 37], as shown in Fig. 3.6. The available space is rather limited, since the distance between the dipole magnets D2 and D3 is around 1 m. The distance between the accelerator beam pipe and the forward detector is also very small. Such a location results in severe requirements for the tracking system. Due to the closeness to the beam pipe, it must be able to operate at rather high counting rates ($> 10^7 \text{cm}^{-2}\text{s}^{-1}$). In addition, because of the short distance between the MWPCs, one has to

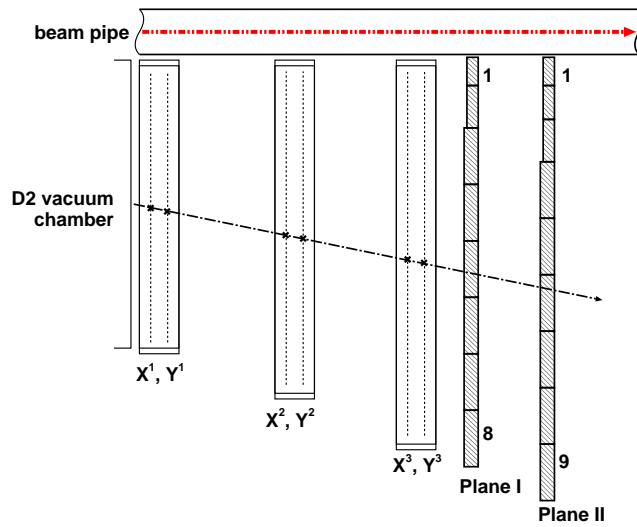


Figure 3.6: Schematic top view of the forward scintillation hodoscope with the typical particle track.

achieve a sufficiently high spatial resolution (better than 1 mm). Such a spatial resolution leads to a momentum resolution of about 1%, which allows one to identify particles reliably. These requirements are fulfilled by the installed and used multi-wire proportional chambers [39, 40].

The forward scintillation hodoscope (FH) consists of two planes with 8 and 9 vertically oriented individual counters, respectively, each of which is read out on both sides (Fig. 3.6). The counters of one plane are shifted by half a counter width with respect to the counters of the second plane. The vertical length of all scintillators are the same while the width gradually decreases towards counters in the high momentum region near the beam pipe, where higher counting rates are expected (Tab. 3.3). The scintillators are viewed from both ends via light guides with PMTs of the types XP 4222 (51 mm diameter) and XP 2972 (23 mm diameter) for the 20 mm and 15 mm counters, respectively. The counters, being independent units, are assembled in a common frame. In the forward direction, each hodoscope covers some momentum range for forward emitted protons. Fig. 3.7 shows the momentum

Table 3.3: Dimensions of forward hodoscope

Layer	FH number	height [mm]	width [mm]	thickness [mm]
I	1	360	40	15
I	2	360	60	15
I	3 - 8	360	80	20
II	1	360	40	15
II	2	360	50	15
II	3	360	60	15
II	4 - 9	360	80	20

acceptance in the forward direction.

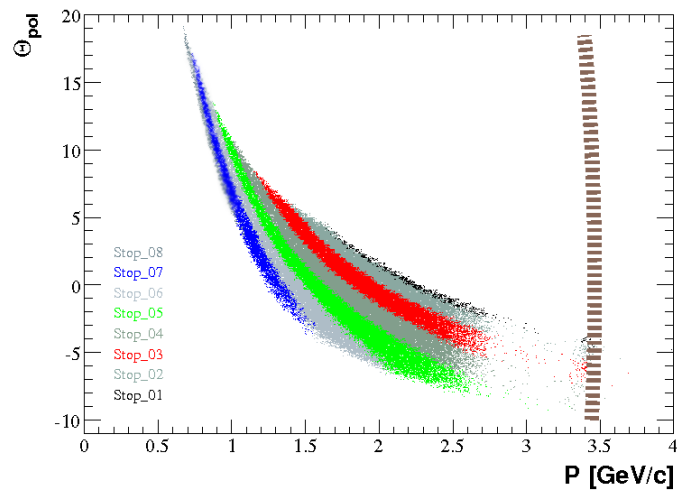


Figure 3.7: The angular *vs* momentum acceptance of the FDS. Different colors indicate different STOP counters.

3.3 *Electronics and Data Acquisition*

Digitization of the signals from the scintillation and Cherenkov detectors is performed with CAMAC (FERA) and FASTBUS QDC- and TDC-modules. Readout is initiated by a trigger, based on information on TOF and energy-loss of the ejectiles. With one specially built VME-module for each STOP counter it is possible to set a common TOF gate (length variable between 3 and 23 ns) in coincidence with up to 16 individually adjustable START-STOP combinations [47]. Sixteen of these modules are needed for the ANKE TOF(PDS) trigger, which can select pions, kaons or protons within about 70 ns, and are used for a first reduction of e.g. pions and protons in the PDS already on trigger level. For the necessary decision time, the analog signals are delayed by 60 m long coaxial cables (300 ns). The system has been developed by FZ-Jülich and RWTH Aachen. Additional coincidences with forward or negative STOP counters can be applied, if the invested reaction requires e.g. a three particle correlation in PDS, NDS and FDS. Such a three particle coincidence reduce further the trigger rate for the data acquisition system. All scintillator detectors are equipped with LEDs (built at FZ-Rosendorf), which allow one to monitor the pulse heights of the counters and to check the trigger- and data acquisition system (Fig. 3.8). For the MWPCs a highly integrated readout system, based on chips RAL 111 and RAL 118 of the Rutherford Appleton Laboratory, Oxford, Great Britain, is used [51]. The electronics boards are placed directly on the chambers. This readout system was developed at the FZ-Rosendorf, Germany, and the Zentrallabor für Elektronik (ZEL) of the FZ-Jülich [51].

The multi-crate data-acquisition system supports the standard readout systems CAMAC, FASTBUS and VME, designed by the ZEL, FZ-Jülich [52], to meet the requirements of ANKE, e.g. recording of high trigger rates for medium-sized events (< 5 kbyte). For a total trigger rate of 10 kHz, approximately up to 50% of the events are written on tape. The readout time

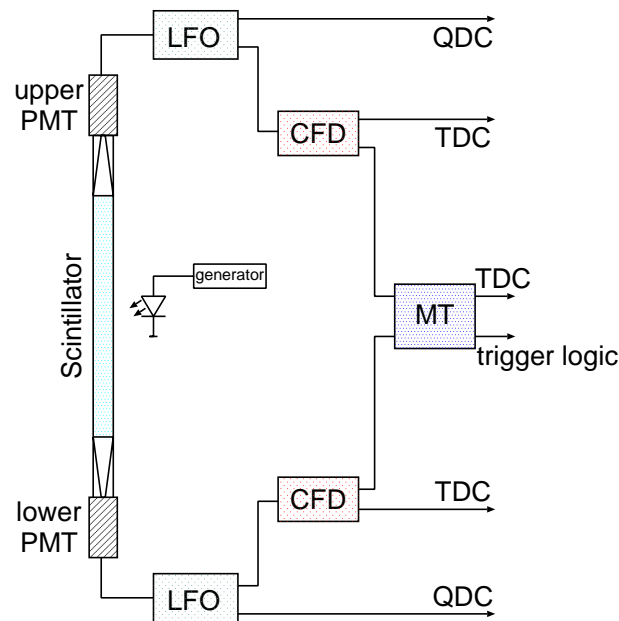


Figure 3.8: Common read out scheme for scintillator counters at ANKE

per event is about 100–150 μs . The crates are read out in parallel using powerful and cost efficient INTEL compatible PC's (single board), running under UNIX (NetBSD). The data are transmitted in clusters of sub-events via a Fast-Ethernet connection to the event builder and are written on a fast DLT tape drive or on a hard disk raid array. In order to ensure the correctness of every event, each readout system employs a synchronization module developed for this purpose. These modules are interfaced by a ring-like bus system. The parallel readout system is scalable over a wide range and is supported by an extensive body of software. The software enables interactive communication with the individual subsystems, which is particularly useful during commissioning and for general diagnostic purposes.

The detector, electronics and DAQ-system as described has been in use for many years at ANKE, and has proven to be very reliable.

3.4 *Experimental Settings for the Measurement*

The installation of the new negative detection system was finished in winter 2002. The first week of beam time at 2.83 GeV beam energy to study the reaction $pp \rightarrow pp\phi$ was taken in the beginning of March. This short beam time also included time for the commissioning and calibration of the NDS. The amount of data which was useful for analysis has been taken in this beam time during 127 hours (5 days and 7 hours).

Table 3.4: Operating parameters of COSY and ANKE and the measurement time under good conditions.

ε [MeV]	18.5	34.5	75.9
T_{beam} [GeV]	2.65	2.70	2.83
P_{beam} [GeV/c]	3.463	3.515	3.65
f_0 [MHz]	1.577	1.578	1.582
α [degree]	5.9	5.81	5.6
B [T]	1.5675	1.5675	1.5675
Target	H ₂	H ₂	H ₂
Δt [s]	600	315	315
Time [h]	301	127	92

At the next beam time at 2.70 GeV beam energy the measurement was carried out during 1 week in the beginning of April 2002. The duration of useful data taking time was 92 hours (\approx 4 days).

A last measurement of this experiment has been carried out in winter 2004 for 3 weeks of beam time at a beam energy of 2.65 GeV.

The experimental settings of ANKE spectrometer, such as beam momentum P_{beam} , revolution frequency f_0 , ANKE deflection angle α , D2 maximum magnetic field B, hydrogen cluster-jet target and the cycle length during the three beam times are summarized in Tab. 3.4.

CHAPTER 4

DATA ANALYSIS PROCEDURES

The analysis of experimental raw data files was performed within the ANKE event reconstruction software framework called RootSorter [44]. This is an ANKE analysis tool, based on the ROOT platform [45], entirely written in C++. In order to achieve the main goal of the experiment, i.e. to extract total and differential cross sections for the $pp \rightarrow pp\phi$ process at three excess energies, several steps are necessary. In the present chapter the K^+ , K^- and proton selection procedures are described. They rely on time-of-flight measurements and the determination of particle momenta.

ANKE coordinate system

All data have been analyzed in the common ANKE Cartesian coordinate system. With the origin at the center of the D2 dipole magnet gap, the positive X axis (going outward from the accelerator center), the Y axis (directed upward), and the Z axis (parallel to the motion of protons along the equilibrium orbit in the accelerator) form a right-handed Cartesian coordinate system as illustrated in Fig. 4.1. The XZ plane coincides with the horizontal plane.

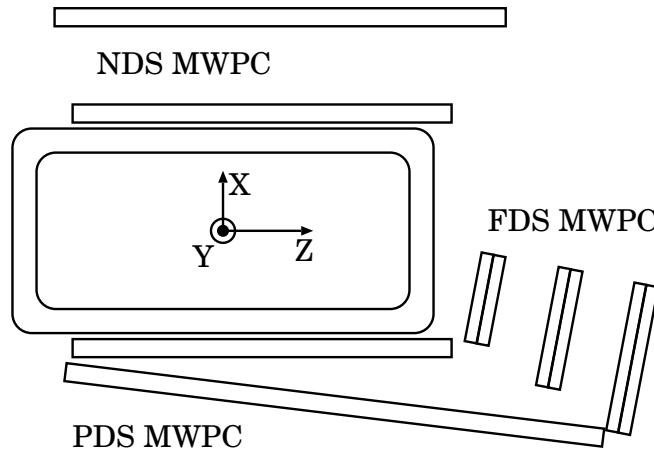


Figure 4.1: ANKE Cartesian coordinate system.

4.1 Event Reconstruction

The event reconstruction code reads the raw events, decodes the detector hits, and generates tracks and particle identification information for each event. The detector calibrations were done using separate codes and the results were taken as input to the event reconstruction software. Efficiencies for all scintillator counters have been tested in laboratory conditions and are considered to be close to 100 %.

4.1.1 Tracking

The position of the track as it passes through a plane is determined by the position of the wire that detects the particle. Finally one point (x, y, z) for each particle in each MWPCs is defined for further tracking. As a track model a straight line in a three dimensional space has been taken. Scattering in the air between the MWPC and inside the MWPCs can be neglected during the track search. Multiple scattering of particles in the 0.5 mm thick aluminum exit window of D2 affects considerably the reconstructed momen-

tum resolution (Sec. 4.1.3). Therefore, the tracks are reconstructed using these space points and a special track reconstruction algorithm depending on the detector system. In addition, adding the distance of closest approach between the track and the wire, small corrections are applied using minimization procedures.

Positive Detector System

The trajectory of a track on the positive side is reconstructed using two multi-wire chambers, each with three wire planes as described in Sec. 3.2. The starting condition for the track search is the START–STOP coincidence

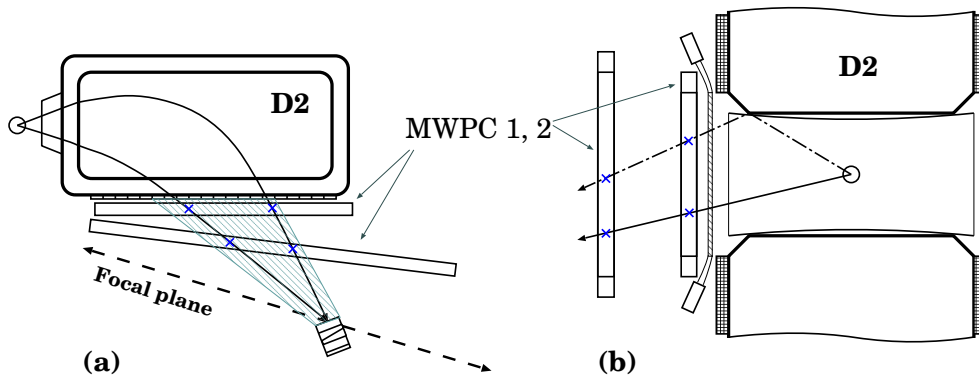


Figure 4.2: Two geometrical cut conditions: Top view (a) for showing START–STOP combinations and front view (b) how to reject rescattered tracks from D2 poles.

at the positive side. The track is reconstructed if at least five different planes (from six) give a signal. However, not all tracks originate from the target. Many of the tracks are due to rescattered from the poles of D2 and from other material in the vacuum chamber.

To reject rescattered background, two cut conditions for horizontal and vertical geometrical restriction are prepared (Fig. 4.2). For a detailed description see Refs. [34, 38].

- First, a hardware level trigger, which is based on a matrix (Fig. 4.3) of

START–STOP combinations allowed within the horizontal acceptance. Since all telescopes are aligned in the focal plane of D2, all particles hitting one of the 15 telescopes fall into a momentum bite of about $\approx 10\%$. This means that for each telescope there is certain set of START counters which can fire if a track is coming from the target.

- In the off–line analysis the YY–correlation in chamber 1 and 2 serves as an additional cut for rejection of rescattered tracks from D2 poles. This cut is used for the vertical acceptance correction. By filling a two-dimensional histograms with Y_1 versus Y_2 coordinates of crossing points for all START–STOP combinations, its parameterization can be used for the selection. The cut is applied within a wide range to avoid cutting of acceptable events.

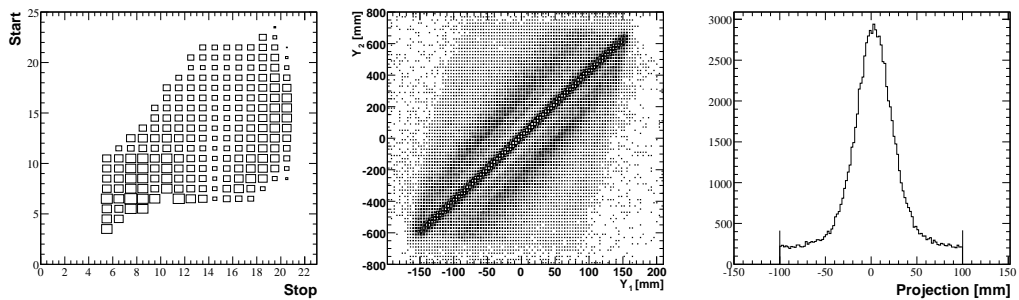


Figure 4.3: Left: START–STOP combinations for the horizontal acceptance cut. Middle: YY–correlation for both chambers and its projection for the vertical acceptance cut at the right figure.

Negative Detector System

The tracks in NDS are triggered using any START–STOP coincidence without any hardware selection unlike in the PDS. So all tracks in the NDS are stored if they are coinciding with PDS and FDS. While the focal plane is far off from available place to install the STOP counters and is behind the

D2 yoke or even the accelerator tunnel, the momentum bite of one STOP counter is much wider than in the PDS. The momentum angular acceptance is shown in Fig. 3.5.

In the off-line analysis both cut procedures are necessary (described in the case of PDS) to separate real tracks from the target. For the separation in the horizontal plane, using experimental data, the matrix of START-STOP combinations has been prepared, similar to PDS and is shown in Fig. 4.4. The YY-correlation in both chambers have been used to reject rescattered background.

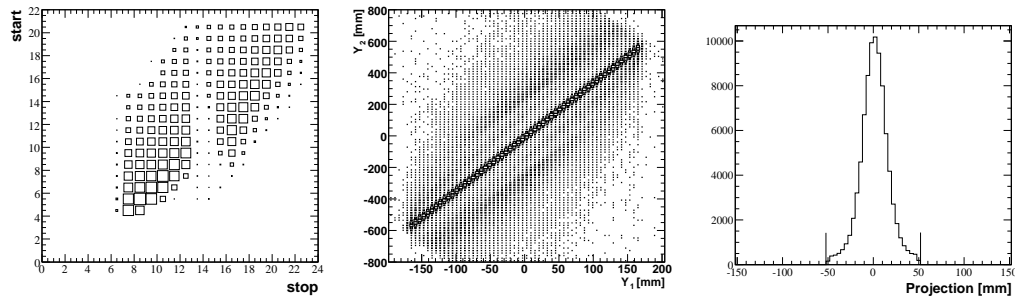


Figure 4.4: Left: START-STOP combinations for the horizontal acceptance cut. Middle: YY-correlation for both chambers and its projection for the vertical acceptance cut at the right figure.

Forward Detector System

The track reconstruction procedure, developed for the ANKE Forward and Side chambers, is described in detail in Ref. [37]. Upper and lower PMT coincidence signal are required for tracking in the forward system. The three planes determine three horizontal and three vertical track coordinates and a track is defined as a straight line. Here the four cut conditions for tracking are used and they are working in the following sequence:

- The track must hit a certain scintillator in FDS hodoscope which has

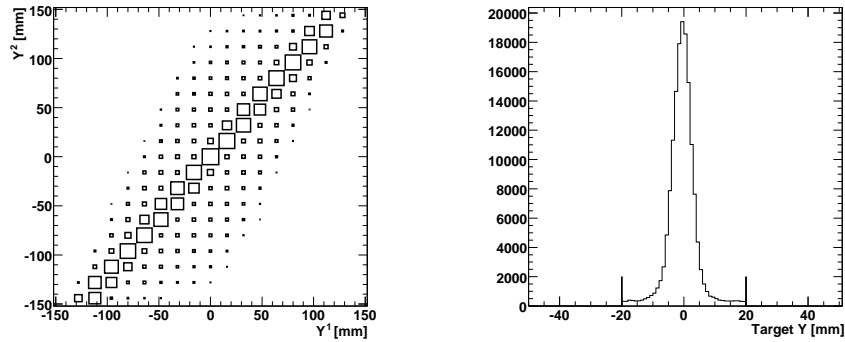


Figure 4.5: Left histogram shows YY–correlation for the forward direction and the right figure is the target distribution in Y direction.

fired and was the input for the tracking trigger. Tracks which hit wrong scintillators behind the chambers are rejected.

- The crossing point for tracks at the exit window must be in an active area, where true tracks are expected. Tracks crossing the exit window outside this area are rejected.
- In analogy to the side chambers, the YY–correlation can be constructed and a two dimensional histogram is filled. After projection of two-dimensional to one dimensional histogram, the cut region can be found. Using this cut rescattered background from D2 poles can be rejected.
- The final condition is to find the target distribution in the Y direction at the measured target point.

Typical histograms for the demonstration of the procedures are shown in Fig. 4.5.

4.1.2 Determination of Chamber Efficiencies

To correct the number of events for each detector system, the detection efficiency has been determined using experimental data.

Positive Detector System

The K^+ detection efficiency for each START–STOP combination, using the TOF and delayed-VETO technique, has been estimated. The number of K^+ events collected in the TOF spectra and number of tracks corresponding to these events have been used to calculate the MWPC efficiency for kaon detection for each detector combination. Also the π^+ efficiency has been

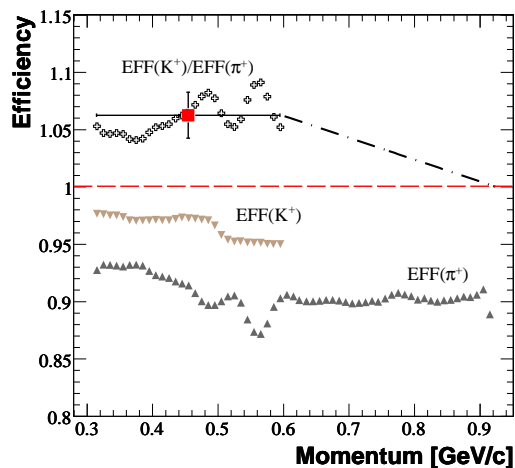


Figure 4.6: Detection efficiency for K^+ and π^+ mesons. Also the ratio of K^+/π^+ detection is shown and interpolated over the whole momentum range.

measured using START–STOP counters to find the efficiency ratio between K^+/π^+ detection as a function of particle momentum. The average efficiency for pions and kaons is shown in Fig. 4.7.

Negative Detector System

The ratio between K^+ and π^+ can be used to deduce the K^- detection efficiency. Because of the experimental restriction in the NDS, direct identification of K^- mesons using a technique similar to what was used in the PDS is impossible. For this purpose, the π^- detection efficiency was determined using the number of events from TOF spectra with and without track information. Under the assumption that positively and negatively charged mesons at fixed momentum should have the same energy loss in medium, the K^+/π^+ ratio from the positive side can be used (Fig. 4.6).

Forward Detector System

In the forward direction the situation is different because no START counters exist. But, on the other hand, in the forward direction the number of MWPC planes allows to define the efficiency directly from wires and the hodoscope. The efficiency for a certain plane is calculated using the track information which is reconstructed using the other planes. The number of tracks reconstructed for one wire, with and without signal from it, is used to calculate the plane efficiency. Namely, the ratio of these two numbers allows to estimate the efficiency in certain regions. The average efficiency for protons is shown in Fig. 4.7.

4.1.3 Momentum Reconstruction and Resolution

Having obtained the track coordinates, we estimate the kinematical parameters of the particle. The magnetic field of D2 is known on a three-dimensional grid, allowing one to reconstruct the ejectile 3-momenta at the production point by using the track information. A number of momentum reconstruction methods have been adopted for the ANKE detection systems, such as:

- Box-field approximation.

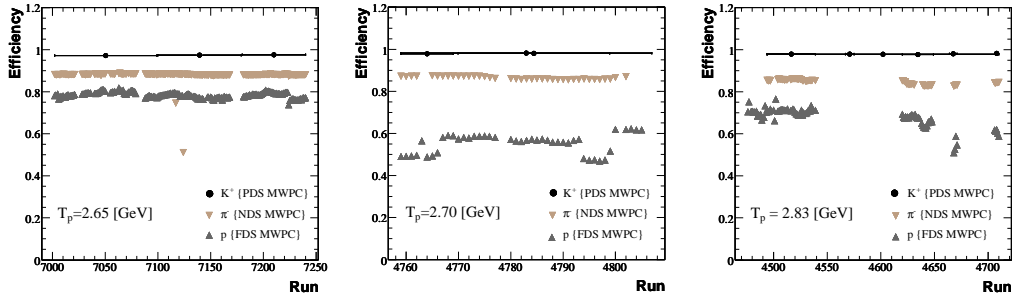


Figure 4.7: The average detection efficiency over one run for different particles for each run is shown for the 3 beam times at 2.65, 2.70, and 2.83 GeV.

- Polynomial approximation.
- Runge–Kutta method.

The box–field approximation has been used on the level of a fast pre-selection procedure of the raw data. In this approach the magnetic field of D2 is approximated by a homogenous box–field with an effective field width and length (X and Y directions, respectively). The particle track inside the magnetic field is defined by the Lorentz force that leads to the circular movement. Outside the magnetic field a straight line is assumed. The vertical and horizontal angles derived from the chamber information are used to calculate components of the particle momentum. The effective length of the box–field is calculated from the magnetic box–field strength, the beam momentum and the ANKE deflection angle. The effective width is determined from experimental data using calibration reaction.

In the polynomial method, each of the momentum components is approximated by a full polynomial of third degree of four-track parameters. The polynomial coefficients are found from a typical sample of events, produced by a GEANT–based simulation program Ref. [46]. The sample is generated for every combination of magnetic field value, the beam direction, and the target position. The details can be found in Ref. [37]. For the selection of pp

elastic events, the polynomial approximation was adopted due to the high speed in the calculations and sufficiently high accuracy.

The Runge–Kutta method has been chosen for the final data analysis due to the better reconstruction accuracy. As initial parameters for tracking from the target, four parameters (P , Θ_{pol} , ϕ_{azi} , Y_{tar}) are used. The target coordinates in X and Z directions are fixed. The initial parameters for the Runge–Kutta is taken from the box–field approximation for PDS and NDS while for the forward part the polynomial method is used.

4.2 Trigger and Data Acquisition Efficiency

In the following the nomenclature of ANKE is listed:

Tel+SW2 — Signal is formed from PDS telescopes or side wall mean timer signals.

FDS/999 — Signal is formed from forward scintillators if at least one of the counters (from any layer) gives a mean-timer signal.

For the first measurement at 2.83 GeV beam energy, four triggers were run in parallel:

- **T1–(Tel+SW2) & (FDS OR).**
- **T2–(Tel+SW2) & NDS.**
- **T3–FDS/999.**
- **T4–10 Hz scaler.**

At the beam energy of 2.70 GeV three different triggers were run in parallel:

- **T1–(Tel(K⁺)+SW2(K⁺)) & NDS.**

- **T2-FDS/999.**
- **T3-10 Hz scaler.**

The last beam time, a three-week measurement at 2.65 GeV, has been done using three parallel triggers:

- **T1-PDS(K⁺) & NDS.**
- **T2-FDS/999.**
- **T3-10 Hz scaler.**

Because of the high pion to kaon ratio for some of the kinematic settings, we require the event to pass some particle identification time-of-flight cuts before generating a trigger. In order to have a high efficiency for detecting kaons, we accepted a trigger as a positive kaon if it passed a certain combination of positive START-STOP counters. The hardware time-of-flight trigger using information of the positive telescopes has been adjusted. The TDCs are mainly used as latches, telling which signals were present when the trigger was taken. This allows us to determine what kind of event formed the trigger. In all measurements with triple coincidence, the trigger was used without any prescaling.

The FDS trigger was used for luminosity determination, as discussed in Sec. 5. This trigger selects mainly single protons in the forward direction. Due to the high count rate of pp elastic events, this trigger has been prescaled by three orders of magnitude.

In addition to the spectrometer information, some beam related quantities were read out on the T3 trigger basis. Also the Beam Current Transformer (BCT) information values were recorded as described below in Sec. 5.5.3.

4.2.1 Data Taking Efficiency

All analog signals produced by the detectors take some time to process, which becomes more significant when the count rates are high. Processing and writing of one event takes $\tau_{dt} \approx 100\text{--}150 \mu\text{s}$ and, consequently, during this “deadtime” the processing of any new event signal is inhibited. At low count rates this effect is small, but it becomes more important as the count rate increases. At ANKE there are three sets of positive counters (scalers) for the measurement of the dead time correction. The scalars allow us to look at raw rates and obtain for certain types of electronics problems in the intermediate steps of trigger formation. We also use the scalars to measure computer and electronics dead time by comparing the number of triggers that were formed with the number that were accepted. As monitor scalars, the PDS telescopes from 2 to 5 with dedicated coincidence scheme, have been used. The electronics scheme is shown in Fig. 4.8. The coincidence schemes

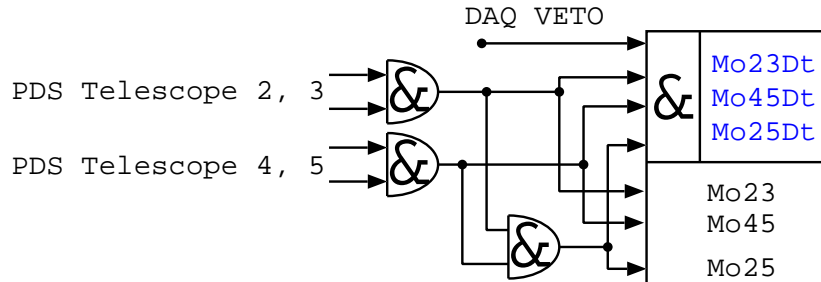


Figure 4.8: Sketch of electronics scheme to monitor the DAQ efficiency using experimental data. DAQ trigger is switched to “1” when the data writing is on.

between 2–3, 4–5 and from 2 to 5 were constructed and written ten times per second on tape using a latched 10 Hz trigger.

In this way the data taking efficiency¹, using experimental data, has been measured. The gate for the limited event counter only accepts events that

¹Also called “dead time correction”.

fall within the DAQ gate window, and in addition inhibits any event that arrives outside this window. From the knowledge of the event counters, it is possible to calculate the effects of the deadtime and hence reconstruct what the count rate should be. For the same channels the coincidence trigger with data taking trigger has been prepared. The fraction of missed events is equal to the fraction of the time the computer is busy. The ratio between monitor counters with and without DAQ trigger were calculated for each run to define data taking efficiency.

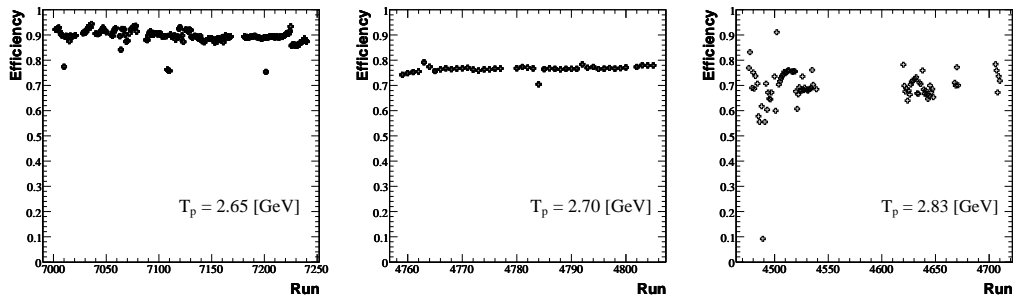


Figure 4.9: The average DAQ efficiency for each run is shown for the 3 beam times at 2.65, 2.70, and 2.83 GeV. Deviations at the high energy are due to an unstable target thickness over time while at the other energies it has been stable.

4.3 Particle Identification

In this experiment there was a large pion–proton background, up to three orders of magnitude higher than the kaon rate. Loose cuts on the TOF counters were used to reject pions on the trigger level during experiment, and tighter cuts were applied in the off-line analysis.

4.3.1 K^+ Selection

To define the K^+ peak position and its width in the summed TOF spectra for further cut, the delayed VETO technique has been used. The TOF between STOP and VETO counters can be effectively used for discrimination against pions and fast scattered proton background. The VETO counters register the delayed decay products of the stopped kaons and this is used for K^+ identification with $\sim 13\%$ efficiency. A typical spectrum for one telescope is shown in the left histogram in Fig. 4.10. The prompt peak is caused by pions that can penetrate the telescopes. Demanding a delayed VETO signal (indicated by the dashed area), an effective suppression of pions can be achieved, whereas stopped kaons can survive due to their exponential decay time. In the right histogram in Fig. 4.10 the normalized TOF spectrum over

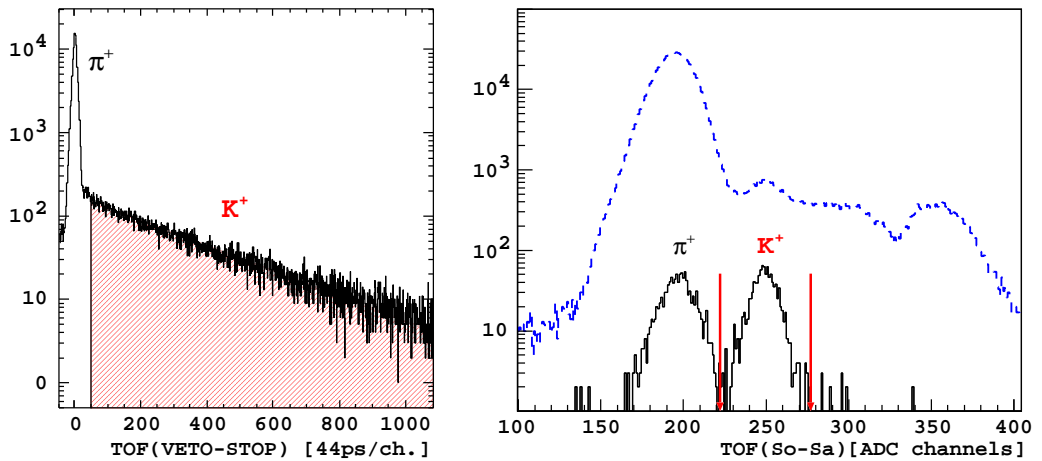


Figure 4.10: Left: TOF between VETO and STOP counters is shown. Right: Normalized TOF over all START–STOP combination is shown.

all START–STOP combinations of PDS, which cover the horizontal emission angles for K^+ particles, is shown. The dashed histogram is the raw spectrum for the three-particle coincidence trigger. The solid histogram shows the remaining events inside the gate for the VETO counter. With precise time information (~ 600 ps FWHM) for the START–STOP TOF (achieved by

constant fraction discriminators and mean timers) the best discrimination between π^+ and K^+ is achieved when kaons just penetrate the ΔE counters and are stopped in degrader II (Fig. 3.2). In Fig. 4.10, the dashed line without any selection criteria pions, protons and an indication on kaon peak is seen. With delayed VETO the signal of the kaon peak is clearly seen and a cut on the TOF spectra can be applied. The arrows on the kaon peak show the gate used for the preselection of kaons without demanding a delayed VETO signal. The peak position is located at channel 250 and σ is equal to 9 channels. Inside this time corridor, some amount of pions is expected. Requirement of a $K^+ K^-$ coincidence in the positive and negative detection can be used for a better selection of kaon pairs.

4.3.2 *Time-Of-Flight Calibration and Selection*

The TOF calibration is needed to achieve sufficient absolute time resolution for the time separation between pions and kaons on both the negative and positive side. The measured time resolution between the NDS START-STOP counters is about 1 ns, slightly inferior than for the positive particle detector. This is due to experimental difficulties for the START and STOP counter construction. This time resolution is insufficient to differentiate between π^- and K^- with momenta above 500 MeV/c.

For the time calibration, an open X^+X^- trigger, which accepts mainly $\pi^+\pi^-$ events, has been measured during several hours. The trigger was set up such that the start signal for the TDC modules is always derived from the STOP counters at the positive side. This allows an absolute time calibration of the negative detector system using the track length and momentum information. Selection of a π^+ particle by TOF between positive START-STOP counters shows very small background contribution. After rejection of rescattered background by tracking, only π^- events remain on the negative side. The reconstructed momentum of $\pi^+\pi^-$ pairs can be used to calculate

the absolute time difference. This can be compared with the TDC value ob-

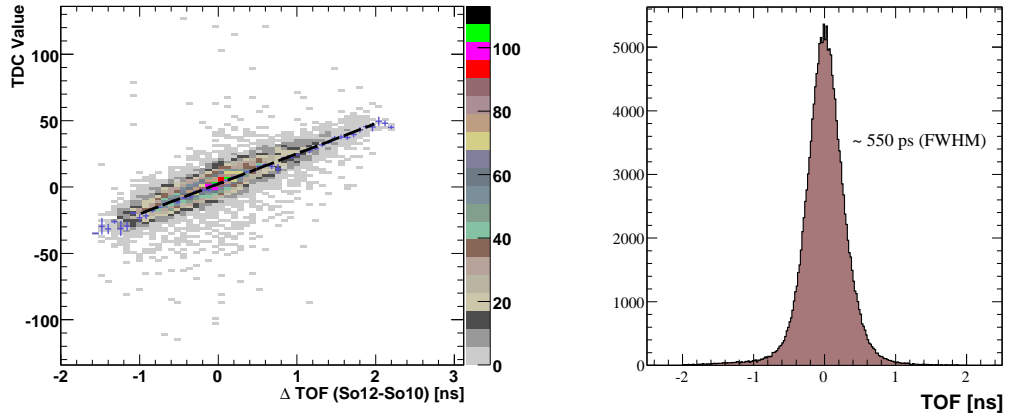


Figure 4.11: Right: TDC value Vs. calculated time difference between NDS and PDS for one STOP-STOP combination using momentum information from $\pi^+\pi^-$ pair. Left: The sum of all normalized TOF difference of the PDS and NDS STOP counters are shown.

tained from the negative counters (Fig. 4.11). The cleanly visible $\pi^+\pi^-$ band can be parameterized by a polynomial. This absolute calibration allows one to identify the negative particle via the knowledge of the two momenta, for a given position. The TOF from the target up to the negative STOP counters follows from the TDC calibration and from the π^- momentum (Fig. 4.11), and shows the difference between these two values. The achieved time resolution is ≈ 550 ps (FWHM) from the TOF histogram. The TOF difference between π^- and K^- from the target to the negative STOP counters are in a range from 1.8 ns up to 5 ns. This allows one to separate K^- events from π^- background over the full momentum range. Using the same technique, the forward hodoscope are calibrated with respect to the negative STOP counters and the time resolution also allows a clear selection of K^-p pairs.

4.3.3 $K^+ K^-$ Correlation

During the experiment the time-of-flight of detected events through the START-STOP difference is measured for each track found in the MWPC chambers. Different tracks may point to different pairs of scintillators, and only those scintillators which are consistent with a track, are included in the TOF measurement. For each scintillator on the track, the TDC values are

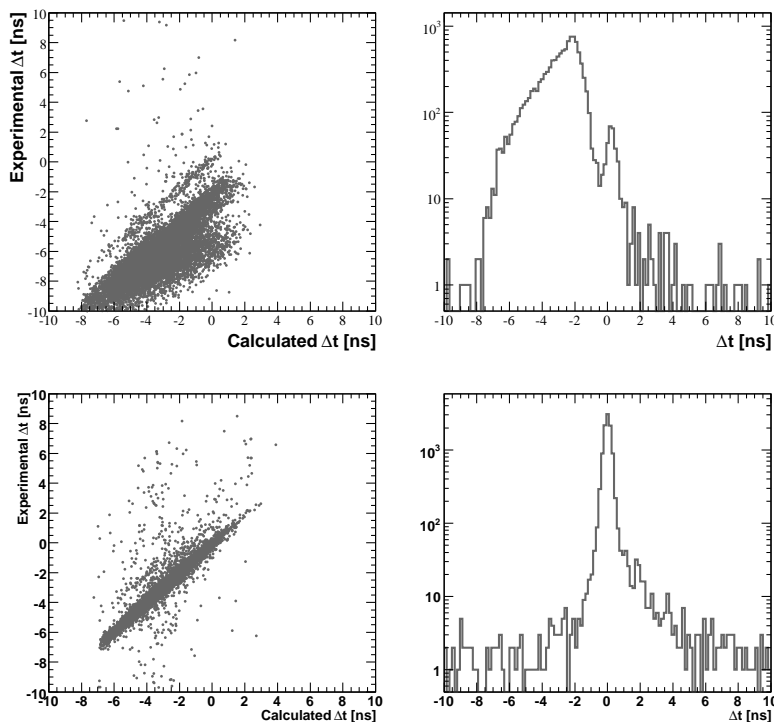


Figure 4.12: The left column shows: the TOF differences between the STOP counter in the negative as well as in the forward detector system with respect to the positive STOP counters versus TOF calculated using momentum information under the assumption that detected particles are K^+K^- and K^+ proton. The right column shows its projection where clear separation between this pair can be performed.

converted into nanoseconds and the times from the two PMTs are combined

if there are two hits to give a time for each scintillator shown in Fig. 3.8. If there is at least one time in the positive system with a certain START–STOP combination and one in the negative side, the time interval is calculated for the tracks. Under the assumption that a K^+ and a K^- are detected, the time-of-flight from positive STOP to target is calculated. Given the time difference of the particle and the momentum (from tracking), the particle mass can be determined, and slow particles can be identified, as shown in Fig. 4.12.

4.3.4 *Missing–Mass Selection*

After selecting K^+ and K^- events, a missing-mass analysis using three detected particles is performed. The distribution at all the 3 energies shows a clear peak at the mass of the proton (see Fig. 4.13). From the width of this peak one can estimate the detector resolution for all the detector systems. Finally, a cut based on the missing mass has been used. The background level below the peak region is estimated to be a 3, 7, and 10 %, respectively.

4.4 *Result for the $pp \rightarrow pp\phi$ Reaction*

In the Fig. 4.14 is shows the resulting K^+K^- invariant mass distributions in the region around $1 \text{ GeV}/c^2$. The $pp \rightarrow pp\phi \rightarrow ppK^+K^-$ reaction is selected by detecting two kaons and one proton. The kaons are identified using TOF between the negative and the positive detector systems, under the assumption that both detected particles are kaons. In this case, protons are always in forward direction and detected using FDS.

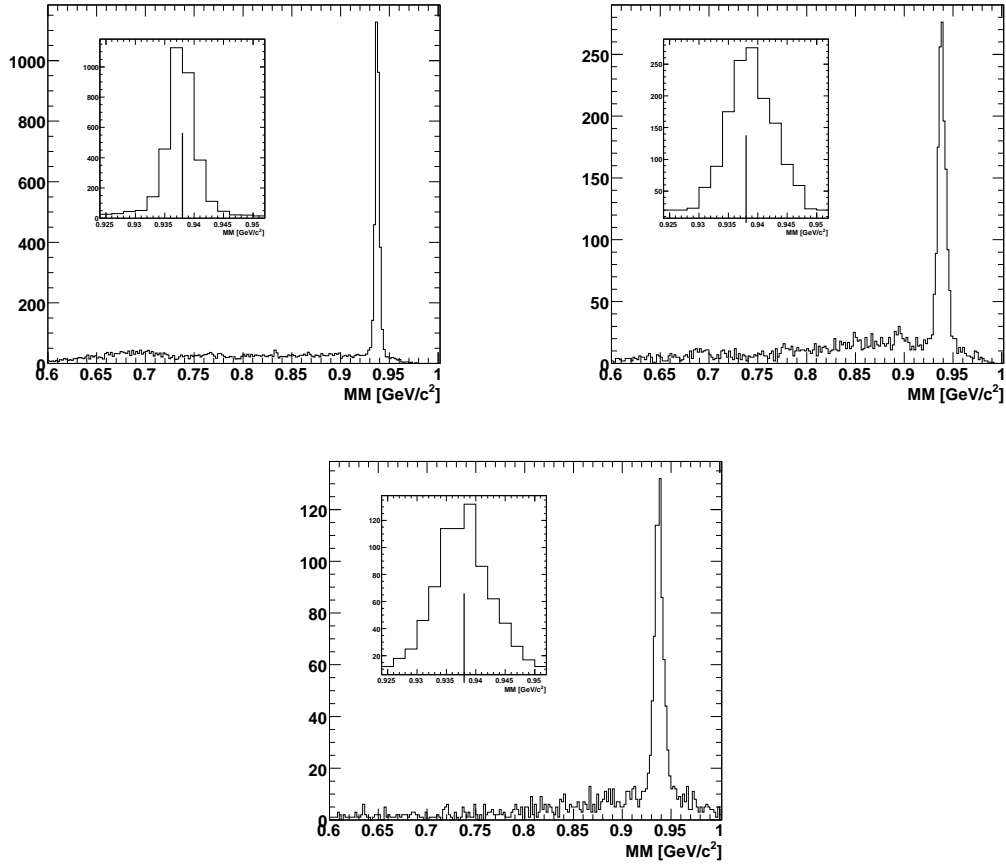


Figure 4.13: Missing mass of pK^+K^- at 18.5, 34.5 and 75.9 MeV excess energies.

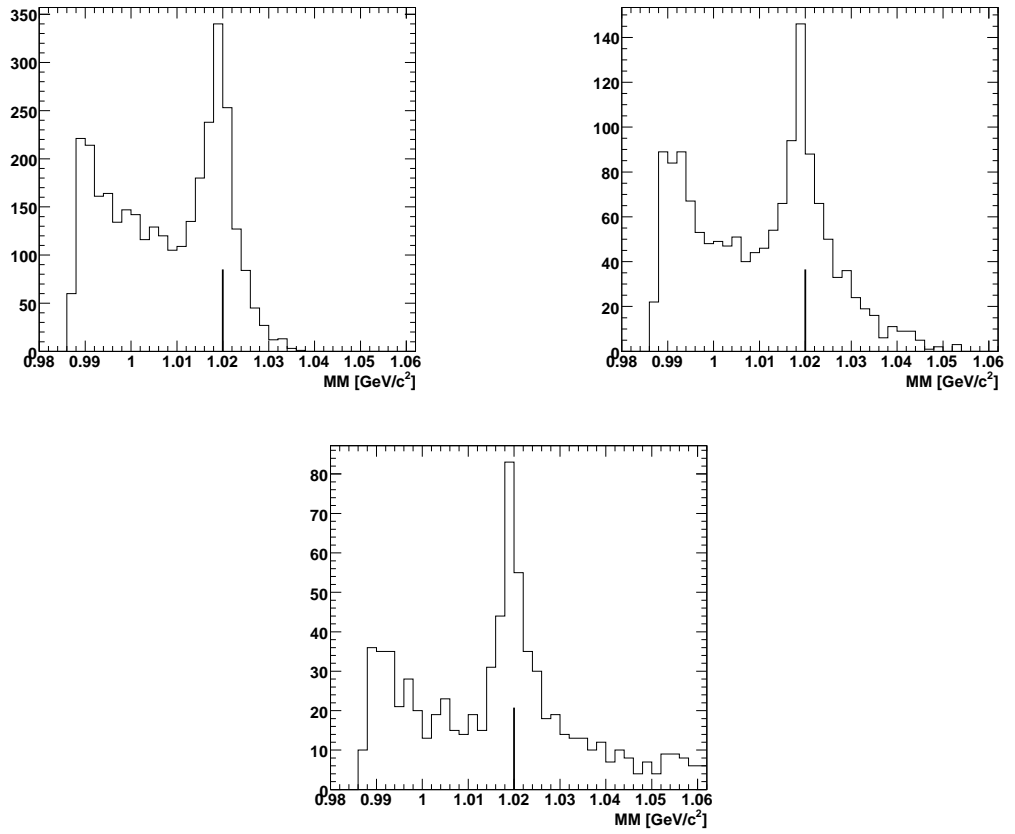


Figure 4.14: Invariant mass of K^+K^- at 18.5, 34.5 and 75.9 MeV excess energies.

CHAPTER 5

LUMINOSITY DETERMINATION

In order to extract the total cross-section for the $pp \rightarrow pp\phi$ reaction, the absolute luminosity must be determined. This has been done using pp elastic scattering for all runs which were used in the analysis. The integrated luminosity over the time is given by the formula

$$L^{int} = \int L dt = \frac{N_{tot}}{\int_{\Omega_{det}} \left(\frac{d\sigma_{pp}}{d\Omega}\right) d\Omega} \quad (5.1)$$

where N_{tot} is total number of elastically scattered protons, $\frac{d\sigma_{pp}}{d\Omega}$ is differential cross-section for pp elastic reaction, Ω_{det} is solid angle of the detector and L^{int} is integrated luminosity over time. The luminosity has been determined using a technique, which is based on the known cross section of elastically scattered protons at small laboratory angles between 4° and 10° . The momentum resolution of the forward detector enables to distinguish elastically scattered particles from other events. In all measurements, the coasting beam without stochastic cooling has been used. As a target the hydrogen cluster jet target was employed. In addition, a cross check of our results have been performed, e.g. measuring the frequency shift of circulating proton beam.

5.1 *pp* Elastic Scattering Cross-Section

An extensive compilation of the *pp* elastic differential cross-section is available from the SAID database up to a proton beam energy of 3 GeV [48]. The *pp* differential cross-section at three beam energies is shown on Fig. 5.1. Usually, the SAID predictions don't assign errors, but in this case an error

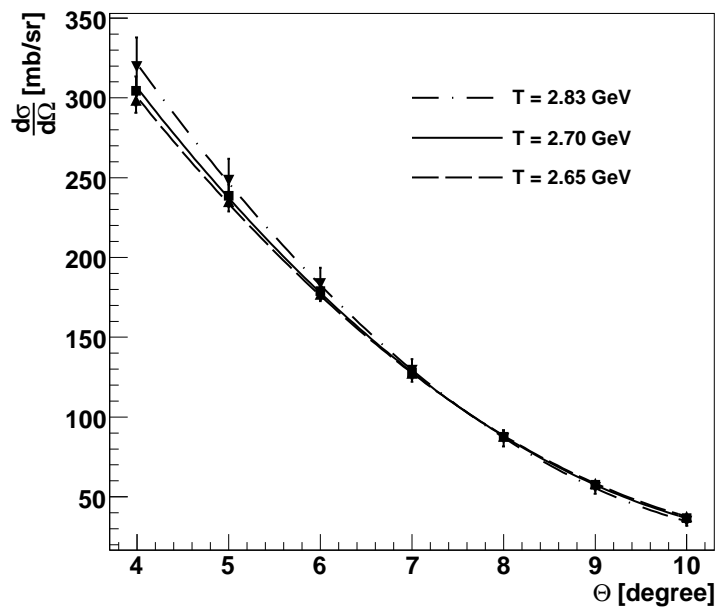


Figure 5.1: The SAID differential cross-section at three beam energies for proton-proton elastic scattering. Angular range from 4° to 10° degree is equivalent to detector acceptance.

bar estimation for a special single energy solution (SES) was provided by R. Arndt¹. The uncertainties are indicated by the solid symbols with error bars in Fig. 5.1 and are given in Tab. 5.1 for different angles. Finally the SAID data points were fitted using a pol2-function in order to extract functions of the differential cross-sections at all three energies.

¹by private communication

Table 5.1: The numerical values (including errors) of the differential cross-sections are given at all three energies in the angular range corresponding to the ANKE acceptance.

Θ_{pol} [degree]	18.5 MeV $\frac{d\sigma}{d\Omega}$ [mb/st]	34.5 MeV $\frac{d\sigma}{d\Omega}$ [mb/st]	75.9 MeV $\frac{d\sigma}{d\Omega}$ [mb/st]
4.0	298.1±7.99	304.0±9.09	319.3±18.32
5.0	235.0±6.13	238.7±6.99	248.2±13.73
6.0	177.1±4.54	178.9±5.19	183.6±9.91
7.0	127.5±3.29	128.0±3.77	129.2±7.06
8.0	87.97±2.38	87.56±2.72	86.65±5.08
9.0	58.41±1.74	57.59±1.97	55.71±3.72
10.0	37.61±1.28	36.71±1.44	34.65±2.72

5.2 Acceptance for pp Elastic Scattering

At the ANKE experiment, only a small fraction of elastically scattered protons can be detected, mainly due to geometrical restrictions. The forward detector system in this experimental setup is able to detect protons in the forward direction for polar angles from 4° to 10° . In Fig. 5.2 the two dimensional event distributions of azimuthal and polar angles are shown. In this

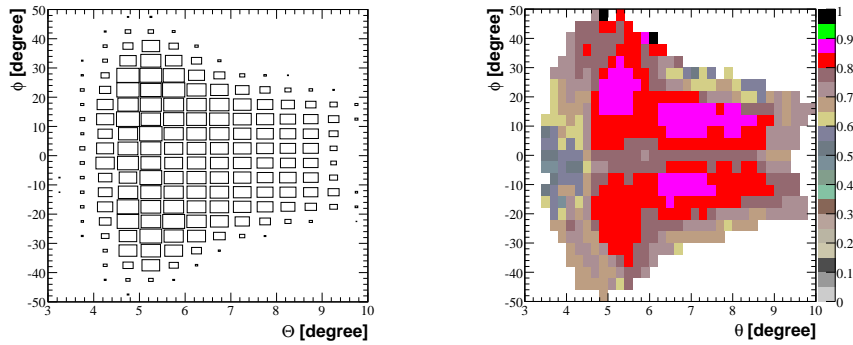


Figure 5.2: Left: Efficiency corrected 2 dimensional histogram of event distribution over the polar and azimuthal angular range. Right: Efficiency map for the forward MWPCs used for luminosity determination.

histogram it is clearly seen that the distribution is symmetrical with respect to the azimuthal angle. For the acceptance determination the detector acceptance has been divided along the horizontal direction into polar angle bins of 0.5° . After that for each polar angular range, the detector solid angle cal-

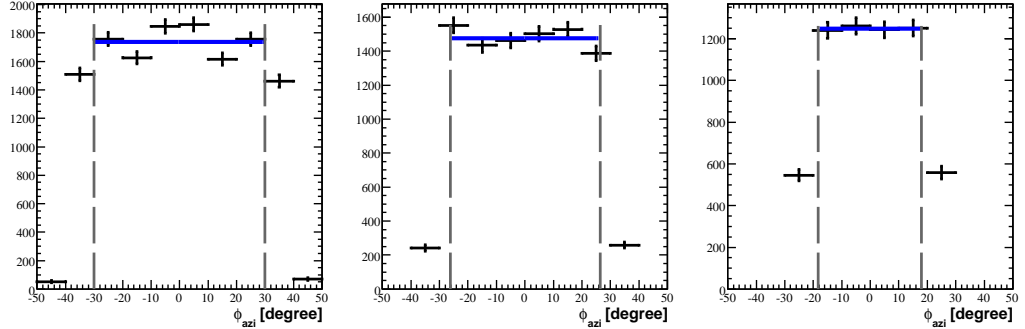


Figure 5.3: Typical histograms to defined detector edges in azimuthal directions for $\Theta_{pol} = 5.25^\circ$, 6.25° , and 7.25° .

culatation has been done. Typical spectra for azimuthal angular distributions are shown (Fig. 5.3) in order to define experimentally, edges for azimuthal angles. Finally for each slice of polar angle the geometrical acceptance was calculated using Eq. 5.2.

$$A_i = \Omega_i^{det} = \Delta\phi_i [\cos\Theta_i - \cos(\Theta_i + 0.5^\circ)] \quad (5.2)$$

where Ω_{det} is solid angle of the detector.

5.3 Selection of *pp* Elastic Scattering

As mentioned before, our general method to define luminosity is based on the well known *pp* elastic reaction. The data of *pp* elastic scattering were taken

simultaneously with the ϕ data, but the trigger was prescaled in order to avoid blocking of the main trigger. Approximately 20% of total events in the forward detectors are pp elastic, and they cover only first four counters as shown in Fig. 3.7. Because pp elastic scattering has a very large cross-

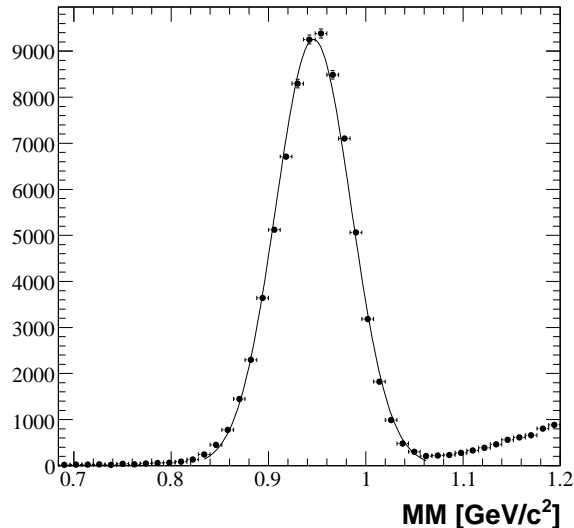


Figure 5.4: The proton missing mass spectra.

section and is not suppressed much by the geometrical acceptance, it is easily observed in the proton missing mass spectra. The momentum resolution of the ANKE FDS enables a good separation from the background. To separate elastic events from the inelastic background, the scattered particle was assumed to have same mass as proton², and the missing mass was calculated as shown in Fig. 5.4. The events are divided into angular bins with steps of 0.5° in order to plot the angular distribution. Elastic events have been extracted for each angular bin, where the azimuthal distribution has a smooth isotropic shape in the acceptance. In these histograms, bins are already corrected for the MWPC efficiency. For the detector efficiency cor-

²Protons in this case are scattered from beam or from target.

rection of these data, two-dimensional efficiency maps for each MWPC plane were created. Each track, which was filled in these histograms is weighted using these two dimensional efficiency maps. Typical spectra of missing proton mass for several angular ranges are shown in Fig. 5.5. The peaks at the

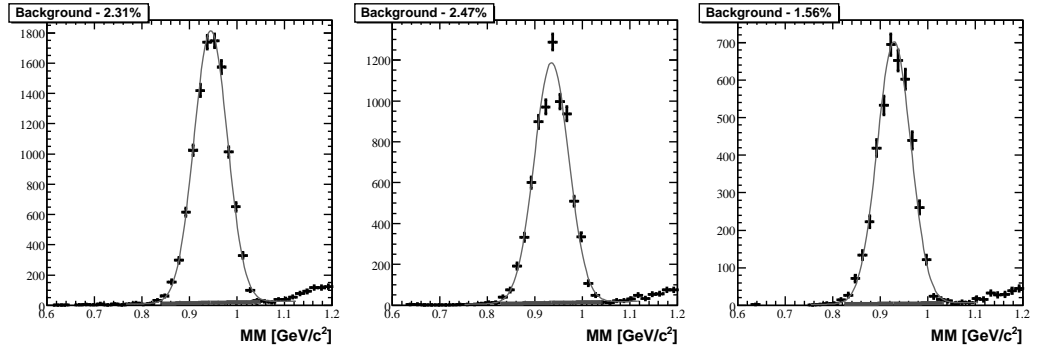


Figure 5.5: Efficiency corrected missing proton mass spectra for $\Theta_{pol} = 5.25^\circ$, 6.25° , and 7.25° . Under the peak dashed area shows background.

proton mass corresponds to elastic scattering and has acceptable background shown in Tab. 5.2. The background has been extracted using the integration of the dashed areas in Fig. 5.5 and the fraction of background is also indicated. Then for each angular range the elastic peak was fitted by a sum of a Gaussian distribution with an inclined line, and events were selected within 3σ from fitted Gaussian parameters. After that, the number of events were corrected by the prescaling factor, with the correction of the DAQ efficiency (described in Sec. 4.2.1) using Eq. 5.3.

$$N_{tot}^{pp} = \frac{N_{det}^{pp} n_p}{\varepsilon_{DAQ}} \quad (5.3)$$

where n_p is prescaling factor for forward trigger and ε_{DAQ} is data taking efficiency.

5.4 Luminosity calculation and error estimation

Finally, using count rates and differential cross-sections derived from SAID data, corrected for the FDS acceptance, the luminosity for the different polar angle bins was determined. By fitting of angular distribution points with a differential cross-section function using one parameter, the luminosity has been determined (Fig. 5.7):

$$\frac{d\sigma(\Theta)}{d\Omega(\Theta)} = C_L \frac{dN_{tot}^{pp}(\Theta)}{d\Omega^{det}(\Theta)}, \quad C_L = \frac{1}{L^{int}}$$

The uncertainties for each beam energy are shown in Tab. 5.2.

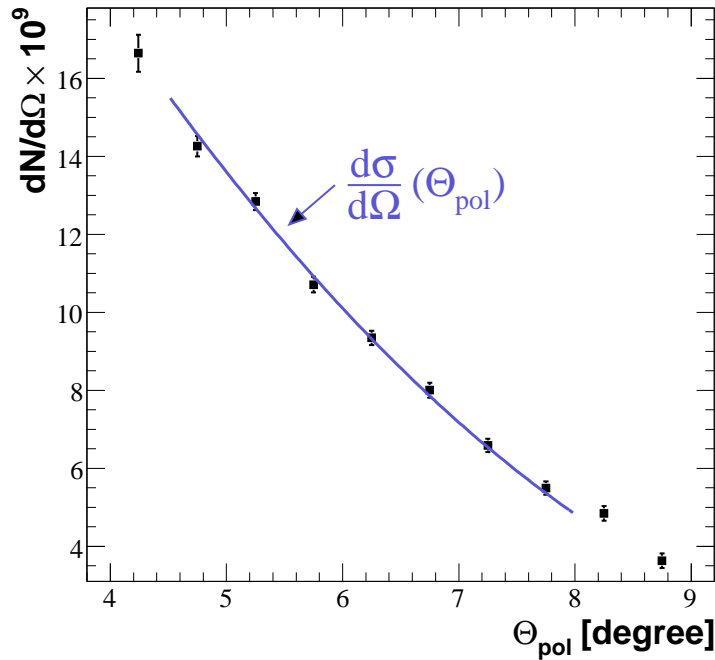


Figure 5.6: Angular distribution at excess energy of 18.5 MeV. The fitting function is the differential cross-section for the same beam energy. There is one fitting parameter which is used to calculate the luminosity.

Table 5.2: Systematical uncertainty for luminosity determination via pp -elastic scattering. The uncertainty marked by * is not included in total error.

Systematic uncertainty	18.5 MeV	34.5 MeV	75.9 MeV
MWPC efficiency*	$\pm 5\%$		
SAID data base	$\pm 3\%$	$\pm 3\%$	$\pm 6\%$
Acceptance correction*	$\pm 8.2\%$	$\pm 7\%$	$\pm 7\%$
Momentum reconstruction	$\pm 1\%$	$\pm 1\%$	$\pm 1\%$
DAQ efficiency	$\pm 5\%$	$\pm 5\%$	$\pm 5\%$
FDS prescaling	$< 2\%$	$< 2\%$	$< 2\%$
Background (3σ)	2%	5%	5%
$\Delta L = (L_\theta - L_{Mean})$	$\pm 1.3\%$	$\pm 4.5\%$	$\pm 6\%$
Total	$\pm 4\%$	$\pm 6\%$	$\pm 9\%$

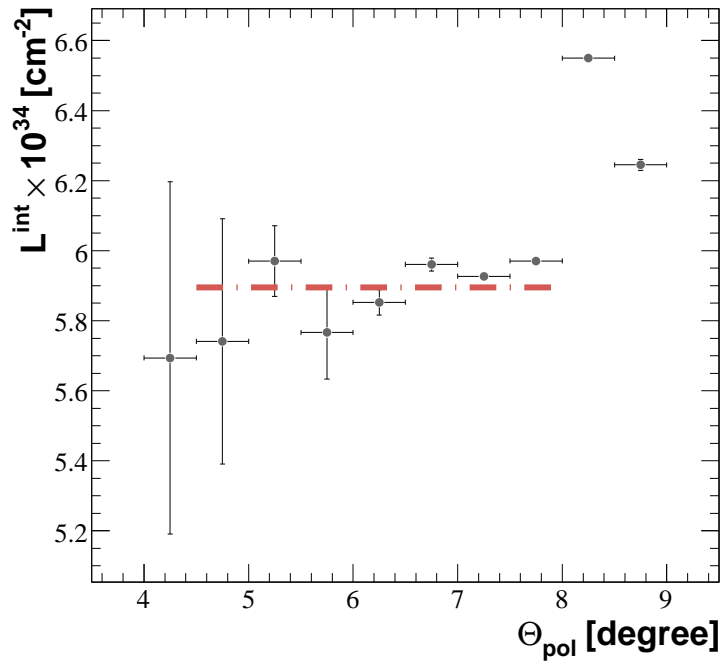


Figure 5.7: Angular distribution at excess energy of 18.5 MeV. The fitting function is the differential cross-section for the same beam energy. There is one fitting parameter which is used to calculate the luminosity.

5.5 *Cross Check via Energy Loss Measurement*

The target density N_t was obtained by measuring the frequency shift of the stored proton beam as it lost energy due to its repeated passages through the target. Combined with the measurements of beam current J_b (5.5.3) this yielded the value of luminosity. In this method the luminosity is obtained by multiplying area density of the target with the simultaneously measured proton beam flux. It is important to mention here that the shape of the beam–target overlap plays an important role.

$$L = N_t \cdot J_b \tag{5.4}$$

where J_b is the average flux of incident beam particles and N_t the average area density of the target particles over one cycle.

5.5.1 *Measurement of the Target Thickness*

The energy loss dT per single traversal, divided by the stopping power dE/dx (given in units of $MeVcm^2g^{-1}$) and the mass of the target protons m ($1.673 \times 10^{-24}g$) yields the number N_t of target atoms per unit area which are interacting with the proton beam (Eq. 5.5). The stopping power has been taken from NIST [50], tabulated for protons in hydrogen, or using the Bethe–Bloch equation. This noted that the numbers obtained by both methods coincide better than 10^{-3} .

$$N_t = \frac{dT}{(dE/dX)m} [cm^{-2}], \tag{5.5}$$

dT can be determined by measuring the energy loss ΔT in a small time interval Δt via the change Δf of the revolution frequency f_0 ($1.577MHz$) of

the ion beam. dT and Δf are related through the Eq. 5.6.

$$dT = \frac{\Delta T}{f_0 \Delta t} \quad (5.6)$$

On the other hand

$$\frac{\Delta T}{T_0} = \frac{1 + \gamma}{\gamma} \frac{\Delta p}{p_0} \quad (5.7)$$

where T_0 (2.65 GeV) and p_0 (3.463 GeV/c) are initial beam energy and momentum. $\gamma = (1 - \beta^2)^{-1/2}$ is the relativistic variable, Lorentz factor.

$$\frac{\Delta p}{p_0} = \frac{1}{\eta} \frac{\Delta f}{f_0} \quad (5.8)$$

where η is the so-called off energy function connecting the relative frequency change with the relative momentum change.

Equations 5.6, 5.7 and 5.8 can be combined in a single expression for N_t (5.5)

$$N_t = \frac{1 + \gamma}{\gamma} \frac{1}{\eta} \frac{1}{(dE/dX)m} \frac{T_0}{f_0^2} \frac{\Delta f}{\Delta t} \quad (5.9)$$

5.5.2 Determination of η by a Measurement of the Compaction Factor α

The measurement is realized by changing of the magnetic field of the COSY dipoles which are driven by a single power supply unit. The η -parameter can be calculated using 5.10 formula:

$$\eta = \gamma^{-2} - \alpha \quad (5.10)$$

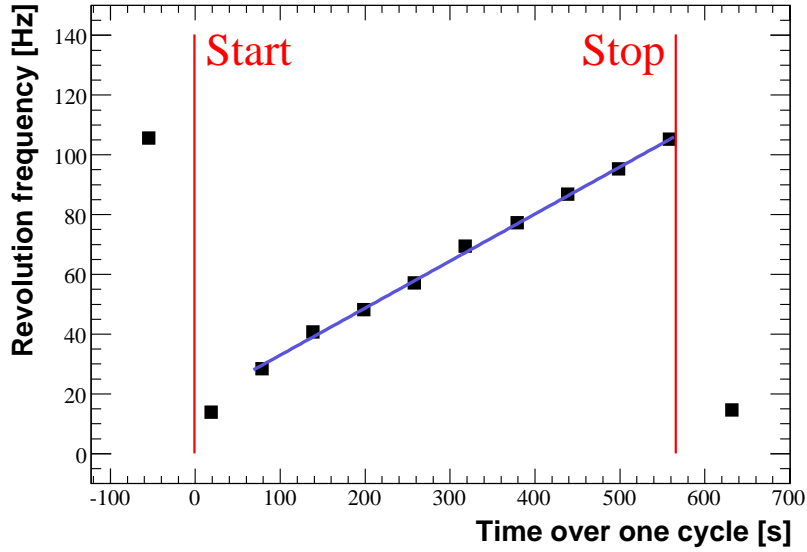


Figure 5.8: Average frequency shift ($\frac{\Delta f}{\Delta t}$) of the center of gravity of the Schottky spectra over one cycle. Red lines shows where the cycle have been started and where it was finished.

where η is the off-energy function described as in Eq. 5.8.

$$\frac{\Delta f}{f_0} = \alpha \frac{\Delta B}{B_0} \quad (5.11)$$

5.5.3 Measurement of the Ion Flux

The flux is obtained by dividing the electric ion beam current I_b by the electric charge of the ion:

$$J_b = \frac{I_b}{q_p} [s^{-1}], \quad (5.12)$$

The current I_b is measured by a high precision beam current transformer (BCT) [Ref.]. The instrument is calibrated to deliver a voltage signal of

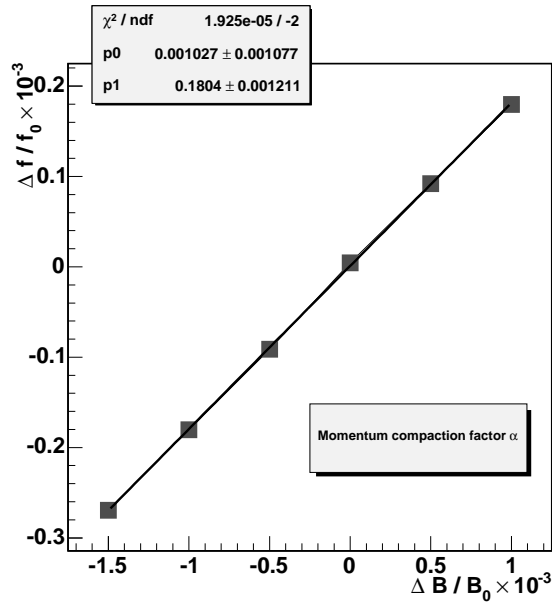


Figure 5.9: Relative change of f_0 versus relative change of the dipole field.

100 mV for a 1 mA beam current. Via an ADC the BCT signal was continuously recorded by the ANKE data acquisition system. The accuracy of the BCT is specified to be 0.01%. Fig. 5.10 shows the proton beam current for a sequence of successive cycles. Within each cycle the beam current is slightly decreasing due to beam losses in the ring. Also the initial beam current is varying a bit from cycle to cycle. Therefore, the mean value of ion beam has to be determined for each cycle.

5.6 Luminosity calculation and error estimation

While in ANKE data acquisition system the end of the run, mostly don't coincide with end of the cycle. The average frequency shift ($\frac{\Delta f}{\Delta t}$) can not be extracted from fitting of all points (see Fig. 5.8).

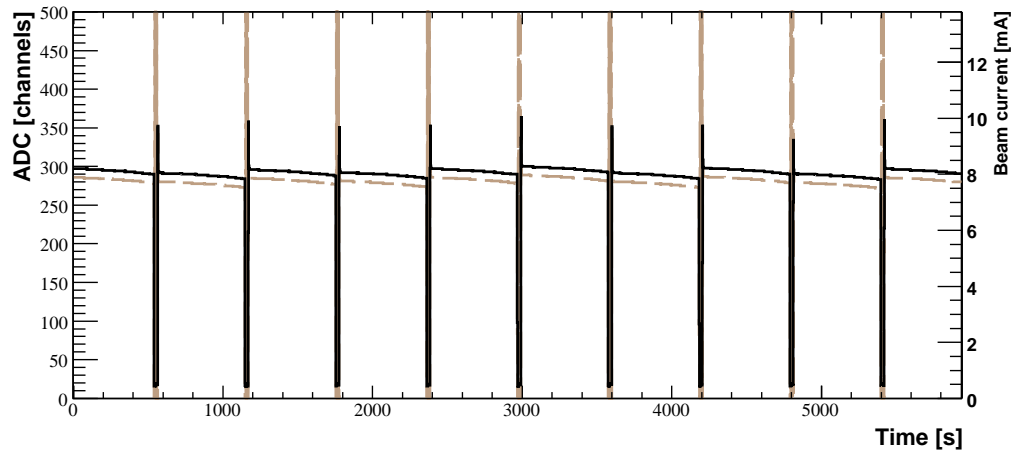


Figure 5.10: The beam current measured at two different points of COSY ring. Solid line shows the BCT signal from device located close to ANKE experiment while dashed line is from device close to EDDA experiment.

Finally integrated luminosity has been determined using the sum of the start counts:

$$L^{int} = L' \times \frac{SOS_{tot}}{SOS'}$$

where SOS_{tot} is the integrated counts of the PDS START counters over whole run and SOS' is integrated PDS START counts inside the cycles where the target density have been estimated.

Possible error sources of the measurement, especially residual gas influences, were carefully studied resulting in a relative accuracy of better than 10%.

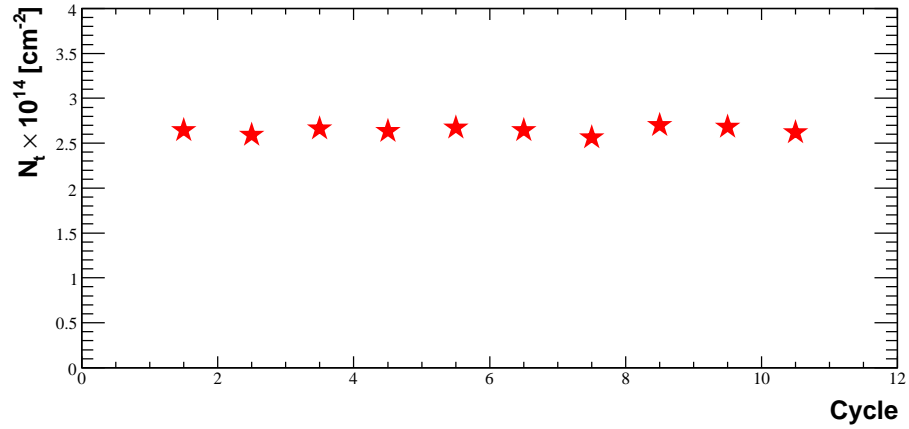


Figure 5.11: Typical values for target thickness during one run.

Table 5.3: Error estimation for the Schottky method

	typical value	syst. err.
frequency shift rate [Hz/s]	~ 0.167	$< 4\%$
η parameter	-115	$< 2.5\%$
systematic residual gas effect	$\sim 6\%$	$\pm 3\%$
specific energy loss [$MeV cm^2 g^{-1}$]	4.108	$\sim 1\%$
BCT signal [mA]	~ 15	$< 1\%$

5.7 Results

Summarized luminosity over whole beam time for each energy is tabulated in Tab. 5.4. The statistical and the systematic uncertainties are also listed. The results at lowest energy where the both methods have been used do compare reasonably well. Both methods coincide within the error limits, however, it is obvious that there is a constant systematic deviation of $\sim 30\%$ between both methods.

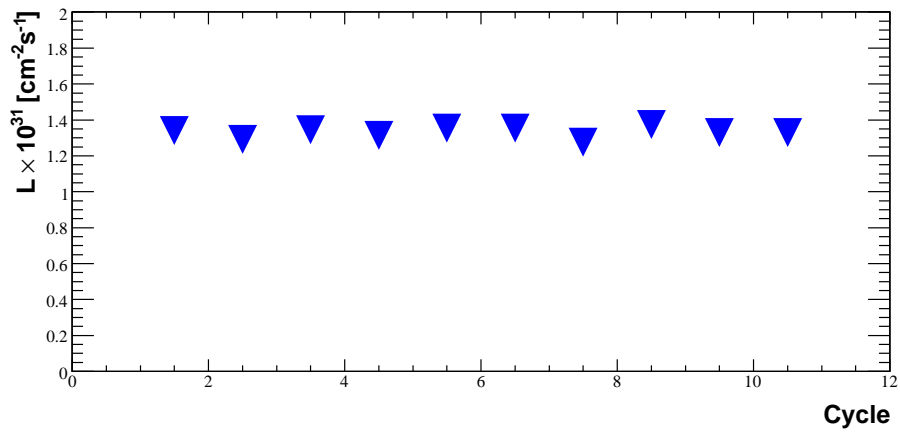
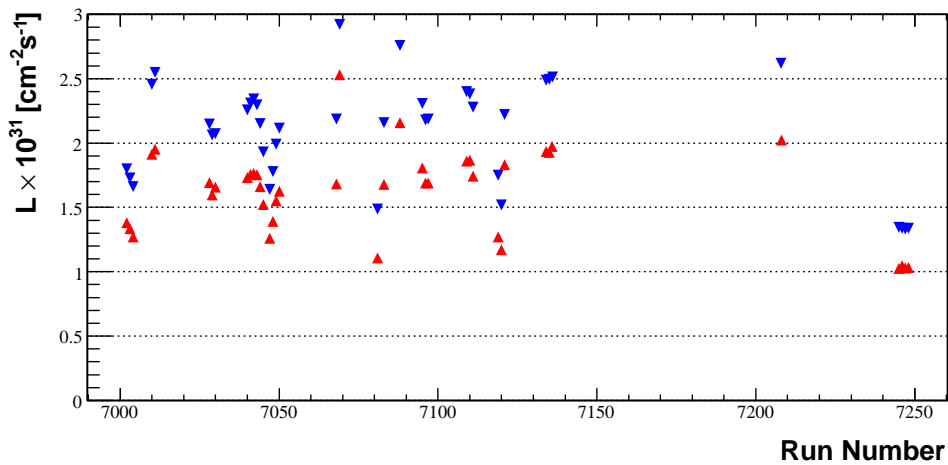


Figure 5.12: Typical values for luminosity during one run.

Table 5.4: Integrated luminosity.

T_p [GeV]	$\int \mathbb{L} dt$ [μb^{-1}]	err. stat.	err. syst.
2.65	1.924796×10^7	1%	4%
2.70	0.969063×10^7	1%	6%
2.83	0.635107×10^7	1%	9%

Figure 5.13: Comparison of the luminosity determined by the Schottky method \blacktriangledown and by elastic scattering \blacktriangle .

Part III

Physics Results

CHAPTER 6

RESULTS AND DISCUSSION

In order to determine cross sections the detector acceptance must be included. The event numbers and target and beam intensities have been obtained and are given in the previous chapters. Finally in the following the experimental results are presented and discussed.

6.1 Acceptance Determination for $pp \rightarrow ppK^+K^-$

The differential acceptance of ANKE has been obtained with the Monte Carlo method described in Ref. [30], which allows one to determine the acceptance independent of the ejectile distributions at the production point. For an unpolarized measurement 16 degrees of freedom (dof) parameterize the ppK^+K^- final state completely. Numerous constraints exist which significantly lower the total number of independent dof. For instance, the particle identification and 4-momentum conservation reduce the number of dof to 8 if the reaction proceeds in two steps, i.e. $pp \rightarrow p_1p_2\phi \rightarrow p_1p_2K^+K^-$. In this case, five variables can be used to describe the three body system, and only three degrees of freedom are further required to uniquely determine the decay of the intermediate ϕ state. Under the assumption that the production of the

final state should be symmetrical around the beam direction, in fact 7 dof are sufficient. A three dimensional matrix for the acceptance correction has been used [54]. The relative momentum of the two protons p_{pp} in the final state and the polar angle Θ of the daughter K^+ mesons in the rest frame of the K^+K^- system have been chosen for two dimensions of the matrix. Close to threshold, for both of these distributions a significant difference from a pure phase space can be expected due to the final state interaction of the two protons and the angular decay of the ϕ vector-mesons (see Fig. 6.3). The third dimension is the K^+K^- invariant mass, which allows, after acceptance corrections, to determine the absolute contribution of ϕ -meson and nonresonant K^+K^- -production. Each of these three variables are subdivided into 10 to 30 bins with a width given in table 6.1. The whole matrix contains

Table 6.1: Kinematic variables and the bin sizes associated with the acceptance correction matrices for the reaction $pp \rightarrow ppK^+K^-$ at three excess energies.

$\varepsilon[\text{MeV}]$	$\Delta M_{inv}^{KK}[\text{MeV}/c^2]$	$\Delta p_{pp}[\text{MeV}/c]$	$\Delta \cos \Theta_X^{K^+}$
19	2.0	0.1	0.2
36, 76	2.0	0.2	0.2

several thousand elements and it was found that the ANKE acceptance is non-zero over all. The matrix has been used to correct the experimental data on an event-by-event basis. Since the ANKE acceptance does not cover all 7 possible dof, the corrections still contain the assumption of isotropic distributions for the remaining polar and azimuthal angles. This assumption is justified, since the Monte Carlo simulation reproduce the measured distributions within the statistical uncertainties (see below).

6.2 K^+K^- Invariant Mass Distributions

The left column of Fig. 6.1 shows the raw $M_{inv}^{K^+K^-}$ invariant-mass distributions in the region of ϕ -meson mass around $1 \text{ GeV}/c^2$ at the three excess energies, and in each of the spectra, a clean ϕ -meson peak is seen on top of a smooth background of nonresonant kaon-pair production. The right column shows the efficiency and acceptance corrected differential cross sections corresponding to $pp \rightarrow pp\phi \rightarrow ppK^+K^-$ events. The latter ones have been used to determine the total cross section for ϕ -meson production and the fraction of the yield due to the nonresonant K^+K^- production. Contributions for misidentified particles have been subtracted using data from outside of the proton peak in the missing-mass distributions (Fig. 4.13) which is also shown in Fig. 6.1. The error bars indicate the statistical uncertainty. The dashed curve shows the estimated nonresonant contribution based on four-body phase-space (ppK^+K^-), whereas the shape of the resonant contribution is given by the natural width of the ϕ -meson folded with a Gaussian ($\sigma \simeq 1 \text{ MeV}/c^2$), in agreement with the momentum resolution of the detector system.

Using the number of ϕ -mesons from the fit, the integral luminosity for the measurement, and the efficiencies and acceptances of the ANKE detectors, the total ϕ -meson production cross section into K^+K^- final state has been deduced for the three energies. The results are given in the Table 6.2 — together with those for nonresonant production.

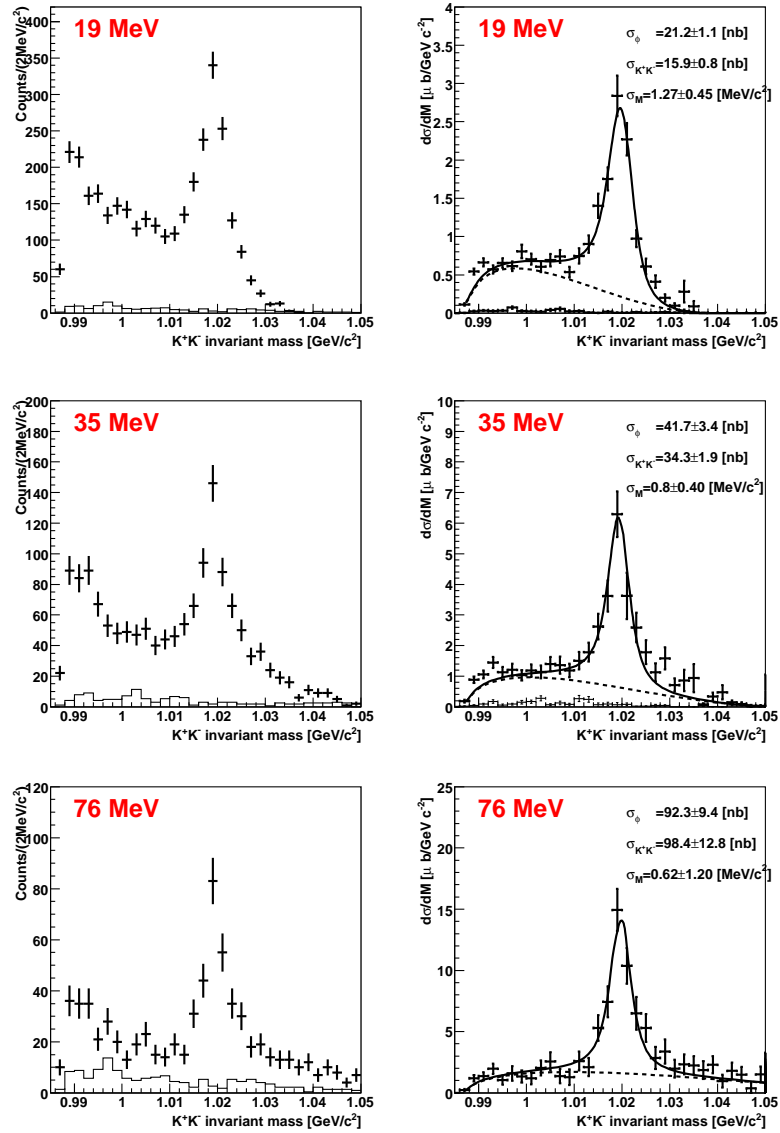


Figure 6.1: Raw (l.h.s) and efficiency corrected (r.h.s) M_{inv}^{KK} distribution for 3 excess energies. The solid histogram shows the background contributions which have been estimated by the side band events in the missing mass distributions of the non-detected proton (described in the text). For the highest energy the misidentified background contribution is already subtracted in the corrected spectrum.

Table 6.2: Total cross sections for nonresonant K^+K^- ($\sigma_{K^+K^-}$) and resonant ($\sigma_{\phi \rightarrow K^+K^-}$) ϕ -productions. The excess energy ε is given with respect to the ϕ central mass value. The cross section errors quoted are statistical (first number) and known systematical (last number) uncertainty.

ε [MeV]	$\sigma_{K^+K^-}$ [nb]	$\sigma_{\phi \rightarrow K^+K^-}$ [nb]
18.5	$15.9 \pm 0.8 \pm 1.9$	$21.2 \pm 1.1 \pm 2.5$
34.5	$34.3 \pm 2.8 \pm 5.5$	$41.7 \pm 3.4 \pm 6.7$
75.9	$98.4 \pm 12.8 \pm 21.6$	$92.3 \pm 9.4 \pm 20.3$

6.3 Cross-Sections

In order to obtain the total ϕ cross section one has to take into account the branching ratio $\Gamma_{K^+K^-}/\Gamma_{\text{tot}} = 0.491$ (see Tab. A.2).

6.3.1 Total Cross-Sections

The final results for the total ϕ -production cross section are tabulated in Tab. 6.3 and plotted as a function of excess energy in Fig. 6.2 together with the data already existing for ω and ϕ meson production in pp collisions ([30, 32, 20, 55, 56, 57]).

In this figure, the lowest energy point at $\varepsilon = 83$ MeV previously measured by the DISTO collaboration is also shown (as a blue ■), and a very good agreement is found with our result at $\varepsilon = 75.9$ MeV.

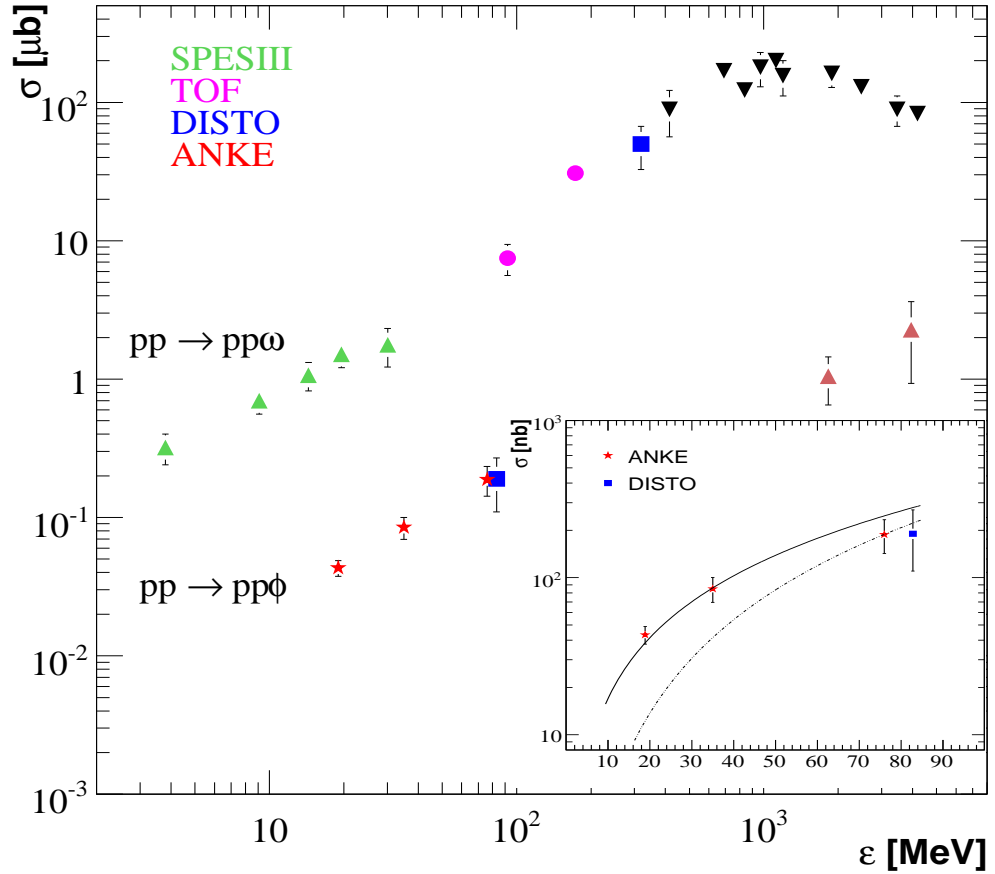


Figure 6.2: Total cross section for ϕ and ω -production in pp collisions as a function of excess energy. The error bars include both statistical and systematic uncertainties. Inset: the dashed line shows a phase space calculation normalized to pass through the highest energy ANKE point, while the solid line, which includes pp final state interaction effects, is a fit to all the ANKE data.

In the Fig. 6.2 the ANKE results are compared with two simple calculations: the dashed line displays the energy dependence of phase space, normalized to the high energy ANKE result at $\epsilon = 75.9$ MeV, while the solid line includes final-state interaction (FSI) effects between the two protons in the 1S_0 state by means of the Jost-function method (see Ref. [53]), scaled

Table 6.3: Total production cross section for $pp \rightarrow pp\phi$ at our three excess energies. In all cases the first number is statistical and the second the systematical error.

ϕ -production (ANKE)		
ε_ϕ [MeV]	$\sigma_{\phi \rightarrow K^+K^-}$ [nb]	$\sigma_\phi(\text{tot})$ [nb]
18.5	$15.9 \pm 0.8 \pm 1.9$	$43.2 \pm 2.2 \pm 5.1$
34.5	$34.3 \pm 2.8 \pm 5.5$	$84.9 \pm 6.9 \pm 13.6$
75.9	$98.4 \pm 12.8 \pm 21.6$	$188.0 \pm 19.1 \pm 41.4$

such that it fits best all 3 ANKE-cross sections. Clearly, the extrapolation of phase-space calculation misses the two low-energy points. The simple Jost-function approach seems to accomplish this, since it describes the energy dependence fairly well and thus it is important to include the proton-proton FSI.

6.3.2 Differential Cross-Sections

Before discussing differential cross sections at the lowest excess energy $\varepsilon = 18.5$ MeV in more detail, it is useful to notice the following constraints: close to threshold, the two final-state protons must be in the 1S_0 state, and the ϕ is in a relative S -wave with respect to this pair. The quantum number of the final state is thus $J^P = 1^-$, which, by conservation of parity and angular momentum, implies that the initial two-proton state is 3P_1 . This in turn requires the alignment of the incident (pp)-spin as well as of the final ϕ -meson spin direction along the beam axis (see Ref. [30] for a more detailed discussion). The polar angular distribution of the decay kaons in the ϕ -meson frame of reference must then display a $\sin^2 \Theta_\phi^{K^+}$ shape relative to the beam direction.

As shown in Fig. 6.3 (upper left panel), the expected behavior is observed: the ϕ 's are produced in S -wave with a (pp)-transition from 3P_1 to 1S_0 . An

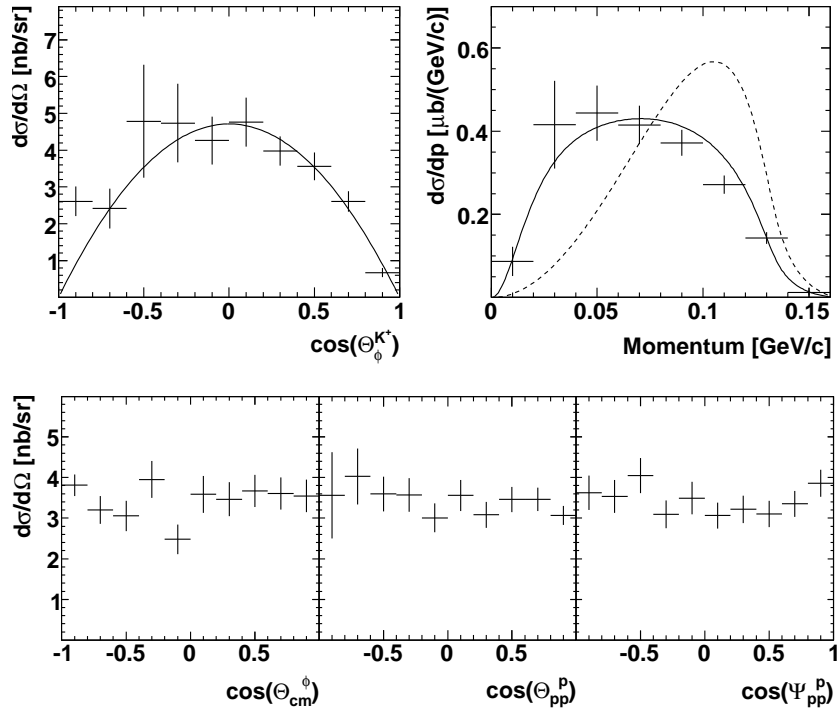


Figure 6.3: Differential distributions for $\varepsilon=18.5$ MeV. Vertical error bars indicate statistical uncertainties and horizontal ones bin widths. Upper left panel: $d\sigma/d\Omega$ as a function of the cosine of the polar K^+ in the reference frame of the ϕ -meson relative to the beam direction. The full line is the expected $\sin^2 \Theta_\phi^{K^+}$ shape. Lower panels: $d\sigma/d\Omega$ vs. cosine of the polar angle of the ϕ meson in the overall c.m. system (left), polar angle of the emitted proton (middle), and proton polar angle relative to the ϕ direction (right), the two latter being in the (pp) reference frame. Upper right: Dependence of the cross section on the pp relative momentum. The dotted line reflects pure phase space whereas the solid includes also the pp FSI.

additional $\cos^2 \Theta_\phi^{K^+}$ contribution, introduced by higher partial waves, is not visible. In the lower part of Fig. 6.3, we show from left to right angular distributions for different angles: (i) the polar angle of the ϕ -meson in the overall c.m. system, (ii) the polar angle of the emitted protons relative to the beam, and (iii) the proton polar angle relative to the ϕ direction. Both proton angles are measured in the (pp) reference frame. All three distributions

are consistent with isotropy and confirm the dominance of the ${}^3P_1 \rightarrow {}^1S_0$ transition.

Finally, in Fig. 6.3 (upper right), the differential cross section is plotted as a function of the proton momentum in the (pp) reference frame. While the phase-space calculation (dotted line) misses the data, inclusion of FSI for the two protons in the 1S_0 -state (solid line) reproduces the experimental result. Thus, a clear and significant pp -FSI effect is observed at $\varepsilon = 18.5$ MeV excess energy.

6.4 OZI Result

In the table 6.4 the data for total cross sections $pp \rightarrow pp\omega$ obtained in the ε range of our measurements are presented for the comparison. The total cross sections for the ω -production at excess energies 19.6 MeV and 30 MeV was measured by **SPES III** and is described in more details in Ref. [20], whereas the data point at an excess energy of 92 MeV was measured by the **COSY-TOF** experiment (Ref. [32]).

Table 6.4: Total production cross section for $pp \rightarrow pp\phi$ at our three excess energies (col. 1) compared to $pp \rightarrow pp\omega$ data in col. 2 [20, 32] at similar excess energies. In all cases the first error is statistical and the second systematical.

ϕ -production (ANKE)		ω -production	
ε_ϕ [MeV]	$\sigma_\phi(\text{tot})$ [nb]	ε_ω [MeV]	$\sigma_\omega(\text{tot})$ [μb]
18.5	$43.2 \pm 2.2 \pm 5.1$	19.6 ± 0.9	$1.51 \pm 0.23 \pm 0.18$
34.5	$84.9 \pm 6.9 \pm 13.6$	30.0 ± 0.9	$1.77 \pm 0.48 \pm 0.23$
75.9	$188.0 \pm 19.1 \pm 41.4$	92	$7.5 \pm 1.9 \pm 1.5$

In the table 6.5 the ϕ/ω production ratios are obtained line by line from the listed cross sections of Tab. 6.4, i.e., at slightly different values of excess

energy (col. 2). Here the statistical and systematical errors are calculated separately. Within the stated uncertainties the ratios are comparable and therefore allow to calculate a weighted mean ratio for the low energy range:

$$R_{\phi/\omega} = (3.0 \pm 0.5) \times 10^{-2}.$$

Table 6.5: ϕ/ω -production ratio indicated by the ϕ excess energies

ANKE ε [MeV]	direct $\sigma_\phi/\sigma_\omega$ $R_{\phi/\omega} \times 10^{-2}$
18.5	$2.9 \pm 0.5 \pm 0.5$
34.5	$4.8 \pm 1.4 \pm 0.9$
75.9	$2.5 \pm 0.7 \pm 0.7$
average	$\sim 3.0 \pm 0.5$

In a second approach the existing ω data were fitted up to $\varepsilon \sim 100$ MeV and from the result (see Fig. 6.4) scaling factors were taken out to scale up and/or down the ω cross sections at the excess energies of the ANKE ϕ measurements. The determined scaling factors are list up in Tab. 6.6, indicated by the changes of excess energies.

Table 6.6: Scale factors for the change of ω cross section to the excess energy of ϕ data.

MeV	scale factor
19.6→18.5	0.94
30.0→34.5	1.14
92.0→75.9	0.77

With the resulting – scaled – ω cross sections the weighted mean ϕ/ω production ratio is:

$$R_{\phi/\omega} = (3.3 \pm 0.6) \times 10^{-2} \sim 8 \times R_{\text{OZI}},$$

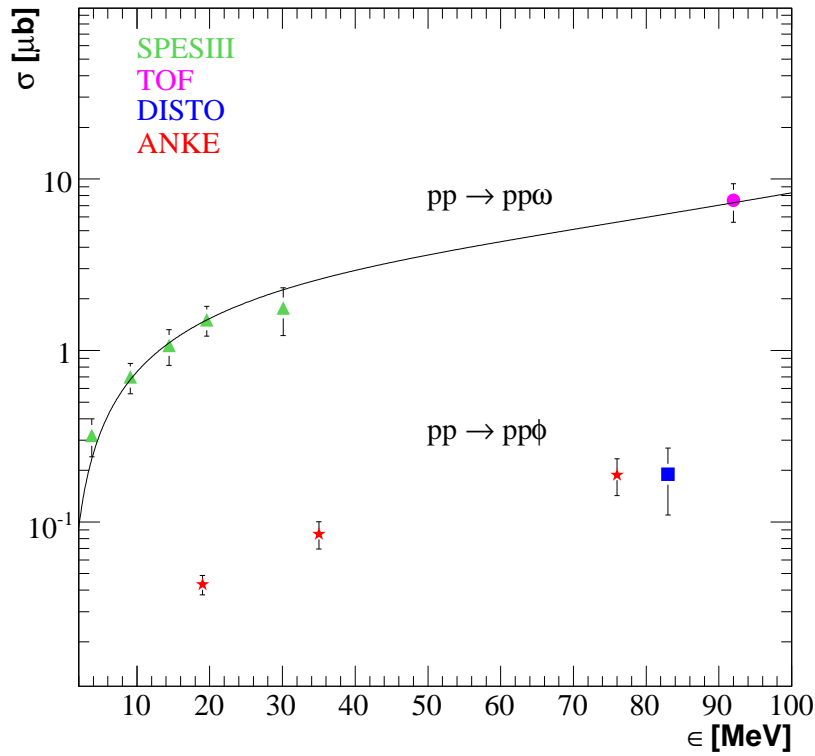


Figure 6.4: Total ϕ - and ω -cross sections in pp collisions below 100 MeV excess energy. The solid line is a fit through the ω data points.

which is 10 % larger compared to the above uncorrected weighted mean, but agrees within the error.

The ϕ/ω ratio at high energy of GeV's is about $\sim (1 - 2.4) \times R_{\text{OZI}}$ (compare Fig. 6.2) and, together with our findings indicate a significant energy dependence of the OZI ratio.

In Fig. 6.5 this is once more graphical illustrated. The three lines show the energy dependence of three-body phase space including the effect of pp final-state interaction (FSI), see Ref. [53]. The dashed line in the middle is normalized to the three ANKE cross sections (stars) at low energies and clearly fails to describe the high energy ϕ data. For comparison the lowest

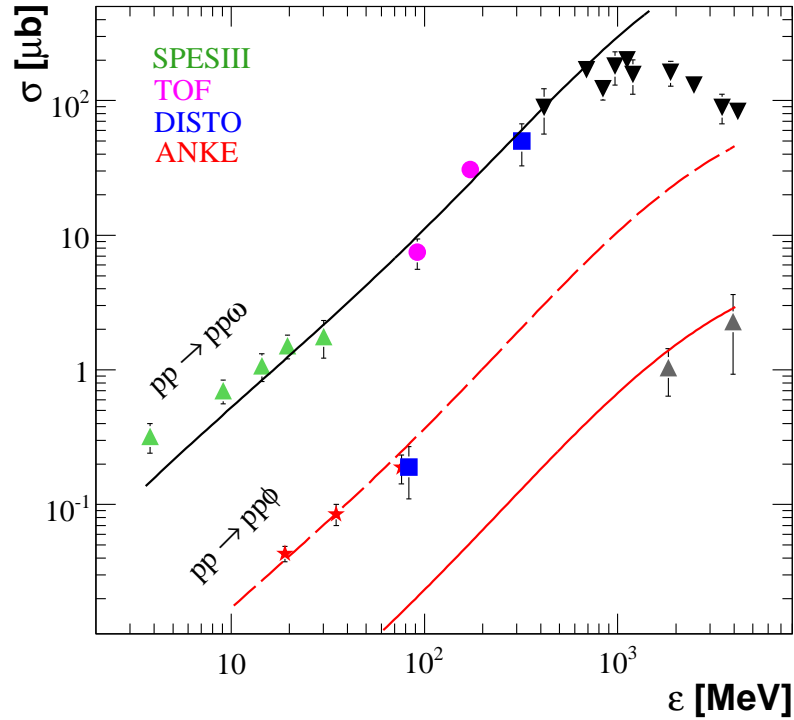


Figure 6.5: Total ϕ - and ω -production cross sections in pp collisions. The three lines show the energy dependence of three-body phase space including the effect of final-state-interaction (FSI) normalized to the ω (top) and ϕ (middle and bottom) cross sections. The middle line is normalized to the three low-energy ANKE points (stars), while the lowest line is fixed by the high energy ϕ cross sections.

line is fixed to pass through the high energy data.

To evaluate the energy dependence of the OZI enhancement factor, it should be noted that the pp production ratio at high energies is in agreement with the experimental ratio $R_{\phi/\omega}$ of $(3.2 \pm 0.8) \times R_{OZI}$ deduced from πN interaction [58]. The latter can be explained in terms of the established OZI violation in the $\phi\rho\pi$ and $\omega\rho\pi$ coupling [59, 60]. The present ratio from near-threshold ϕ and ω production in pp collisions exceeds this value by more than

a factor two. It may be a signal for additional, and as yet non-understood, dynamical effects related to the role of strangeness in few-nucleon systems. This requires more theoretical work to understand its origin and the new ANKE data, with its precision, can contribute to that as a prominent investigation. A first more exotic and speculative explanation has been advanced in Ref. [53]. According to this study a ϕN -resonance contributes significantly to the ϕ production close to threshold and thus the energy dependence of the ϕ cross section as well as the increased OZI ratio is explained. However, the experimental evidence for such a possible resonance is far from certain and will therefore require additional measurements.

6.5 Outlook

At present, from the ANKE data sets, only the 76 MeV data allow to look into the ϕ – *proton* invariant mass distribution, because of the data sets at lower excess energies cover only a small invariant mass range. At present, our limited statistics at 76 MeV of about 200 ϕ events prevents this kind of investigations clearly [61], but a new measurement at 76 MeV has been already performed at ANKE [62] and the statistics of detected ϕ mesons could be improved up to several thousands ϕ 's (see Fig. 6.6). This statistics exceeds the around 500 events detected by the DISTO collaboration and can therefore be used to study more precisely higher partial wave contributions around 80 MeV excess energy. The analysis of these new data is in progress.

In order to study all facets of the ϕ -meson dynamics, it is necessary to investigate the isospin dependence by also measuring the ϕ -production in pn collisions. The investigation of the quasi-free $pn \rightarrow d\phi$ reaction, using a cluster-jet deuterium target (*i.e.* $pd \rightarrow d\phi p_{sp}$), has been recently finished at ANKE and the details of the obtained results can be found in Ref. [63].

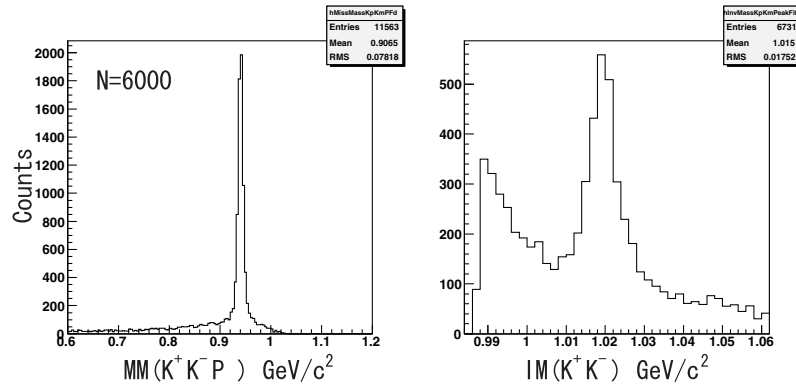


Figure 6.6: New $pp \rightarrow pp\phi$ ANKE data at 75.9 MeV: lhs. shows the missing mass spectrum of the nondetected proton, and rhs. the corresponding K^+K^- invariant mass distribution.

These data allow also to estimate the $pn \rightarrow pn\phi$ cross section using final state theory [63, 64].

Both results, of elementary ϕ -meson production are an important input for the ongoing efforts of understanding the *in-medium* effects on meson properties. In the latter case, ANKE will contribute in the near future by executing an approved COSY-experiment [65]. The aim of this experiment is to study the hadronic ϕ -nucleus and K^- -nucleus potentials via the ϕ and K^- production in $p+A$ reactions. It is expected that the data will permit definite conclusions about the ϕ width in nuclear matter at normal density through the analysis of the A -dependence of the ϕ production cross sections.

Finally, the so called non-resonant K^+K^- production, which is considered the background for the present investigation of (resonant) ϕ -production, needs to be looked at. First of all it may be that a part of the K^+K^- yield may actually be associated with mesonic states (a_0, f_0), and secondly NK final state interactions can be investigated. The corresponding analysis are also in progress.

APPENDIX A

PROPERTIES OF THE ϕ MESON

The ϕ (1020) is a vector meson in the pure $s\bar{s}$ state. The mass, width and corresponding lifetime is given in Tab. A.2 [66]. The K^+K^- decay channel

Table A.1: The ϕ (1020) Meson properties and quantum numbers.

Mass m	1019.456 ± 0.02 MeV
Full Width Γ	4.36 ± 0.05 MeV
Lifetime	20×10^{-23} s
Quantum Number	$I^G(J^{PC}) = 0^-(1^{--})$
Anti Particle	self
S, C, B	0

Table A.2: the ϕ (1020) dominant hadronic decay modes are listed

Decay Modes	Fraction (Γ_i/Γ)	p [MeV/c]
K^+K^-	$(49.2^{+0.6}_{-0.7})\%$	127
$K_L^0 K_S^0$	$(33.7 \pm 0.5)\%$	110
$\rho\pi + \pi^+\pi^-\pi^0$	$(15.5 \pm 0.5)\%$	—
X	1.6 %	—

is dominant among the hadronic decay channels. Naively one would expect the preferred hadronic decay channel ϕ to be pions over kaons, since decay

Appendix A

in pions have much more phase space available. It is to mention here that ϕ decay into two pion ($\phi \rightarrow \pi^+\pi^-$) is forbidden by G-parity conservation.

APPENDIX B

SELECTED NUMERICAL RESULTS FOR LUMINOSITY

Table B.1: The numerical values for Run 7247 analyzed using pp -elastic method.

Θ_{pol} [degree]	N_{tot} $\times 10^9$	ΔN_{pp} [%]	Bg [%]	Ω [steradian]	$L^{int} \times 10^{34}$ [cm^{-2}]
4.75	14.26	1.84	2.08	0.0656	5.72
5.25	12.84	1.70	1.68	0.0836	5.92
5.75	10.71	1.89	2.10	0.0793	5.73
6.25	9.35	1.97	2.07	0.0862	5.86
6.75	8.01	2.39	1.56	0.0644	5.95
7.25	6.59	2.58	1.01	0.0692	5.89
7.75	5.50	3.11	2.07	0.0575	5.99
Total	67.749	2.22	2.071	$0.506 \pm 3.085\%$	5.884

Table B.2: The numerical values for Run 7247 analyzed using Schottky method.

Cycle	Δt [s]	flux $\times 10^{16}$ [s $^{-1}$]	df/dT [Hz/s]	$N_t \times 10^{14}$ [cm $^{-2}$]	$L \times 10^{31}$ [cm $^{-2}$ s $^{-1}$]	$L^{int} \times 10^{34}$ [cm $^{-2}$]
0	534	5.079	0.1563	2.641	1.3418	7.165
1	566	4.978	0.1536	2.592	1.2906	7.305
2	566	5.054	0.1575	2.662	1.3457	7.616
3	566	4.991	0.1559	2.633	1.3144	7.439
4	566	5.075	0.1578	2.668	1.3545	7.666
5	566	5.129	0.1563	2.640	1.3545	7.666
6	566	4.981	0.1519	2.561	1.2758	7.221
7	566	5.088	0.1595	2.699	1.3737	7.775
8	566	4.959	0.1586	2.682	1.3304	7.530
9	507	5.079	0.1550	2.618	1.3299	6.742
Total	5569				1.3300	7.4218

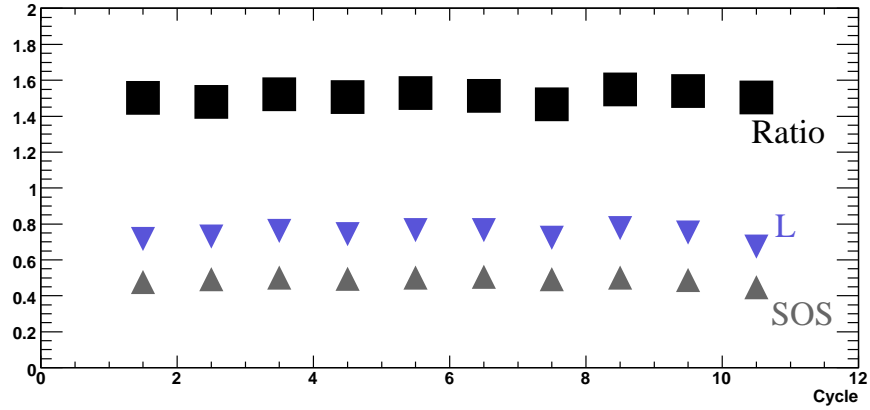


Figure B.1: The ratio between summarized PDS START counts and integrated luminosity derived via Schottky analysis (for Run 7247) is shown in Fig. B.2 with standard deviation less than 2%.

Section B.0

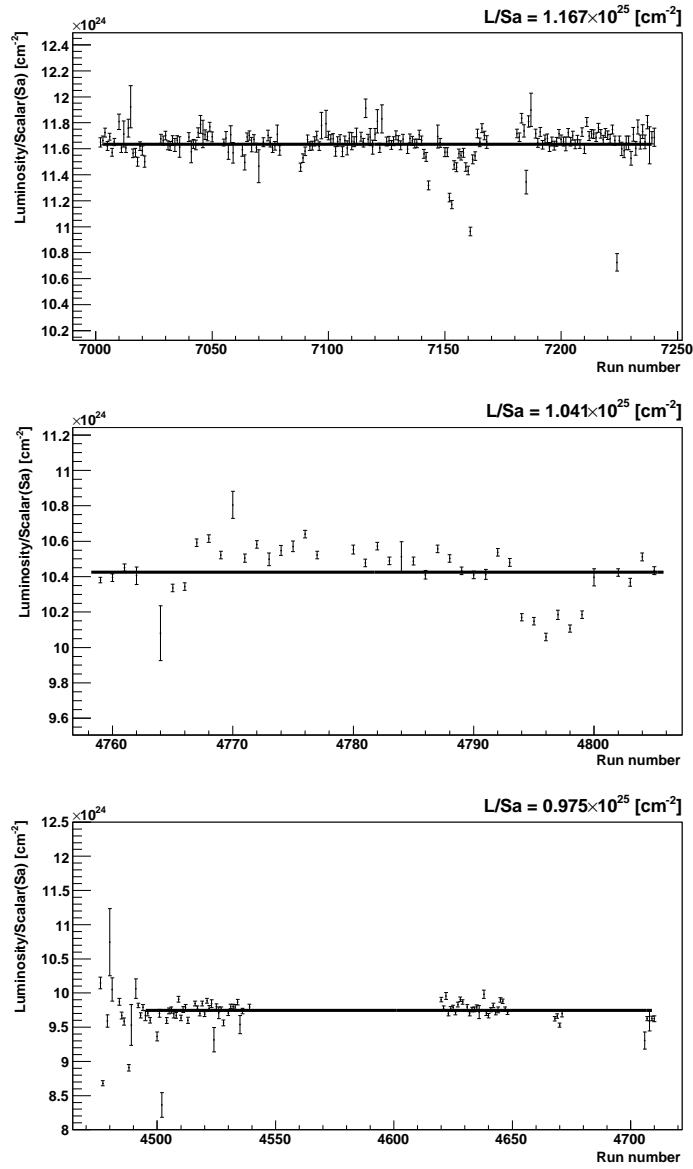


Figure B.2: Ratio between integrated luminosity derived via pp -elastic scattering and sum of PDS START counts at $T_{beam} = 2.65, 2.70$ and 2.83 GeV.

Bibliography

- [1] E. Fermi, C. N. Yang, Phys. Rev. 76, 1739 (1949).
- [2] S. Sakata, Progress of Theoretical Physics 16, 686 (1956).
- [3] M. Gell-Mann, Phys. Lett. 8, 215 (1964).
- [4] Review of Particle Physics ...
- [5] P.L. Connolly et al., Phys. Rev. Lett. 10, 371 (1963).
- [6] S. Okubo, Phys. Lett. 5, 165 (1963).
- [7] G. Zweig, CERN Report No. TH-401 1964 (unpublished).
- [8] J. Iizuka, Prog. Theor. Phys. Suppl. 38, 21 (1966).
- [9] H. J. Lipkin, Phys. Lett. B 60, 371 (1976); current data lead to $R_{OZI} = 3.53 \times 10^{-3}$, see Ref. [10].
- [10] S. Eidelmann et al., Phys. Lett. B 592, 1 (2004).
- [11] A. Sibirtsev and W. Cassing, Eur. Phys. J. A 7, 407 (2000).
- [12] V. P. Nomokonov and M. G. Sapozhnikov, Phys. Part. Nucl. 34, 94 (2003).
- [13] C. Amsler et al., Rev. Mod. Phys. 70, 1293 (1998).

- [14] C. Wilkin; Proc. of 8th Int. Conf. “Baryon’98”, World Scient. Pub. Ltd. ISBN 981-02-3865-7, p.505 (1998).
- [15] W. R. Falk et al., Phys. Rev. C 32, 1972 (1985).
- [16] G. Faldt and C. Wilkin, Phys. Lett. B 382, 209 (1996).
- [17] G. Faldt and C. Wilkin, Phys. Lett. C 56, 2067 (1997).
- [18] J.-F. Germond and C. Wilkin, Nucl. Phys. A 518, 308 (1990).
- [19] F. Hibou et al., Phys. Lett. B 438, 41 (1998).
- [20] F. Hibou et al., Phys. Rev. Lett. 83, 492 (1999).
- [21] E. Chiavassa et al., Phys. Lett. B 337, 192 (1994).
- [22] H. Calén et al., Phys. Lett. B 366, 39 (1996).
- [23] P. Moskal et al., Phys. Rev. Lett. 80, 3202 (1998).
- [24] H. Calén et al., Phys. Rev. C 58, 2667 (1998).
- [25] K. Nakayama et al., Phys. Rev. C 57, 1580 (1998)
- [26] J. Haidenbauer Proc. of 8th Int. Conf. “Baryon’98”, World Scient. Pub. Ltd. ISBN 981-02-3865-7, p.583 (1998).
- [27] S. Barsov et al., Eur. Phys. J. A21, 521 (2004).
- [28] Y. Maeda et al., Submitted for publication (2006).
- [29] S. Okubo, Phys. Rev. 16, 2336 (1977).
- [30] DISTO Collaboration: F. Balestra et al., Phys. Rev. C63, 024004 (2001).
- [31] The CELSIUS Collaboration: H. Calén et al., Phys. Rev. Lett. 80, 2069 (1998); Phys. Rev. C58, 2667 (1998).

- [32] TOF Collaboration: S. Abd El-Samad et al., Phys. Lett. B 522, 16 (2001).
- [33] R. Maier et al., Nucl. Instr. and Meth. A 390, 1 (1997).
- [34] S. Barsov et al., Nucl. Instr. and Meth. A 462, 364 (2001).
- [35] A. Khoukaz et al., Eur. Phys. J. D5 (1999) 275.
- [36] B. Chiladze et al., Part. Nucl. Lett. 113, 95 (2002).
- [37] S. Dymov et al., Part. Nucl. Lett. 119, 40 (2004).
- [38] H. Junghans: *Bestimmung der Impulsspektren von K^+ Mesonen aus Proton-Kern-Reaktionen bei Projektilenergien unterhalb der freien NN-Schwelle*, PhD theses, Köln, 2000; available from <http://www.fz-juelich.de/ikp/anke/en/theses.shtml>
- [39] B. Zh. Zalikhanov et al., IKP FZ-Jülich Annual Report 1993, Jül-2879, Jülich, 1994, p. 57.
- [40] B. Zh. Zalikhanov et al., IKP FZ-Jülich Annual Report 1995, Jül-3200, Jülich, 1996, p. 67.
- [41] K. H. Watzlawik et al., IEEE Trans. Nucl. Sci. 43 (1996) 44.
- [42] M. Hartmann. Ph.D. Thesis, Universität zu Köln 1998.
- [43] A.D. Volkov et al., NIM A 306, 278 (1991).
- [44] V. Hejny et al., *RootSorter: A New Analysis Framework For ANKE*, IKP Annual Report 2002, Jül-4052, 2003.
- [45] R. Brun et al., ROOT: An Object-Oriented Data Analysis Framework, CERN, Geneva, 2003, available from <http://root.cern.ch/root/doc/>

- [46] S. Agostinelli et al., Nucl. Instr. and Meth. Vol. 506, 3, 250 (2003), available from <http://geant4.web.cern.ch/geant4/>
- [47] R. Schleichert. Ph.D. Thesis, Technische Hochschule Aachen, Germany (1996).
- [48] SAID program: R.A. Arndt, W.J. Briscoe, R.L. Workman, and I.I. Strakovsky. http://gwdac.phys.gwu.edu/analysis/nm_analysis.html
- [49] H.J. Stein, D. Prasuhn, IKP FZ-Jülich Annual Report 2001, Jül-3978, Jülich, 2002, p. 64.
- [50] NIST – The National Institute of Standards and Technology, <http://physics.nist.gov>
- [51] W. Erven, K. Zvoll, H. Langenhagen, H.R. Koch and H. Junghans. IEEE Trans. Nucl. Sci. NS-45, 852 (1998).
- [52] M. Drochner, W. Erven, P. Wstner and K. Zvoll. IEEE Trans. Nucl. Sci. NS-45, 1882, (1998).
- [53] A. Sibirtsev, J. Haidenbauer, and U.-G. Meiner, Eur. Phys. J. A (to be published).
- [54] M. Hartmann et al., Phys. Rev. Lett. 96, 242301 (2006).
- [55] A. Baldini *et al.*, in *Numerical Data and Functional Relationships in Science and Technology, Total Cross-Sections for Reactions of High Energy Particles*, edited by H. Schopper, Landolt-Börnstein, New Series, Group 1, Vol. 12 (Springer-Verlag, Berlin, Heidelberg, 1998).
- [56] R. Baldi *et al.*, Phys. Lett. B **68**, 381 (1977).
- [57] V. Blobel *et al.*, Phys. Lett. B **59**, 88 (1975).
- [58] A. Sibirtsev and W. Cassing, Eur. Phys. J. A **7**, 407 (2000).

- [59] M. Gell–Mann and F. Zachariasen, Phys. Rev. **124**, 953 (1961); U.–G. Meißner, Phys. Rep. **161**, 213 (1988).
- [60] S. Eidelmann *et al.*, Phys. Lett. B **592**, 1 (2004).
- [61] M. Hartmann *et al.*, Nucl. Phys. A **755** (2004) 459.
- [62] M. Hartmann *et al.*, COSY Proposal: No. **104.2**, http://www.fz-juelich.de/ikp/publications/List_of_all_COSY-Proposals.shtml.
- [63] Y. Maeda *et al.*, Phys. Rev. Lett. (*to be published*); nucl-ex/0607001.
- [64] G. Fäldt and C. Wilkin, Phys. Lett. B **382** (1996) 209.
- [65] M. Hartmann *et al.*, COSY Proposal: No. **147**, http://www.fz-juelich.de/ikp/publications/List_of_all_COSY-Proposals.shtml.
- [66] K. Hagiwara *et al.*, Phys. Rev. D **66**, 010001 (2002)

List of Tables

1.1	Additive quantum numbers of the three lowest mass quarks and antiquarks. Here, Q is the electric charge in units of e_0 , I is the isospin, I_3 the third component of the isospin, Y is the hypercharge, S is the strangeness, and B is the baryon number. $Q = Y/2 + I_z$, $Y = B + S$	6
1.2	Comparison of experimental masses for the ρ^0 , ω and ϕ mesons.	10
1.3	The ratio $R = \phi X/\omega X$ of the cross sections for production of ϕ and ω mesons in pp , $\bar{p}p$, and πp interactions. P_L is the momentum of the incoming particle. No corrections on the phase space volume difference were made except the cases marked *.	15
3.1	Dimensions of positive START scintillator	30
3.2	Dimensions of negative scintillator	33
3.3	Dimensions of forward hodoscope	36
3.4	Operating parameters of COSY and ANKE and the measurement time under good conditions.	39
5.1	The numerical values (including errors) of the differential cross-sections are given at all three energies in the angular range corresponding to the ANKE acceptance.	63

5.2	Systematical uncertainty for luminosity determination via pp -elastic scattering. The uncertainty marked by * is not included in total error.	68
5.3	Error estimation for the Schottky method	74
5.4	Integrated luminosity.	75
6.1	Kinematic variables and the bin sizes associated with the acceptance correction matrices for the reaction $pp \rightarrow ppK^+K^-$ at three excess energies.	80
6.2	Total cross sections for nonresonant K^+K^- ($\sigma_{K^+K^-}$) and resonant ($\sigma_{\phi \rightarrow K^+K^-}$) ϕ -productions. The excess energy ε is given with respect to the ϕ central mass value. The cross section errors quoted are statistical (first number) and known systematical (last number) uncertainty.	83
6.3	Total production cross section for $pp \rightarrow pp\phi$ at our three excess energies. In all cases the first number is statistical and the second the systematical error.	85
6.4	Total production cross section for $pp \rightarrow pp\phi$ at our three excess energies (col. 1) compared to $pp \rightarrow pp\omega$ data in col. 2 [20, 32] at similar excess energies. In all cases the first error is statistical and the second systematical.	87
6.5	ϕ/ω -production ratio indicated by the ϕ excess energies	88
6.6	Scale factors for the change of ω cross section to the excess energy of ϕ data.	88
A.1	The ϕ (1020) Meson propertis and quantum numbers.	93
A.2	the ϕ (1020) dominant hadronic decay modes are listed	93
B.1	The numerical values for Run 7247 analyzed using pp -elastic method.	95
B.2	The numerical values for Run 7247 analyzed using Schottky method.	96

List of Figures

1.1	Fundamental triplets of (u, d, s) and $(\bar{u}, \bar{d}, \bar{s})$. Y is the hypercharge and I_3 the third component of the isospin (see also Table 1.1).	6
1.2	Baryon octet (left) and meson nonet (right).	7
1.3	Nonet of vector-mesons.	8
1.4	The diagram of $\phi \rightarrow \pi^+\pi^-\pi^0$ decay: via $\phi - \rho$ mixing (left); direct transition to 3π system (right).	11
1.5	ϕ and ω decays: (a, b) allowed (or preferred) by the OZI rule; (c) Forbidden (or disallowed).	12
2.1	One-boson-exchange mechanism for meson production	18
2.2	Total cross sections for meson production in the $pp \rightarrow ppX$ reaction near threshold. Experimental data on the production of η [19, 21, 22], ω [20], and η' -mesons [19, 23] are compared with the predictions of Eq. (2.6) normalized to the η data. The residual scale factors shown are close to unity except in the η' case. The only previously existing data on ϕ production is at $\varepsilon = 83$ MeV [30] and, whereas this is much too high for the S -wave assumptions to be valid, it is amusing that the curve shown for the ϕ does pass through this point. With red stars the new ANKE measurements are included.	22

2.3	Layout of experiments at cooler synchrotron COSY. H^- and D^- ions are preaccelerated in the cyclotron JULIC and injected into the storage ring. In this sketch, four internal and five external experiments are also shown.	26
3.1	Sketch of the ANKE spectrometer and its detection systems. The color lines from target indicates tracks of scattered particles.	28
3.2	Sketch of the ANKE side telescope. It is composed of a STOP, a Cherenkov (only in telescope numbers 7 to 15), two degraders, and ΔE and veto scintillators.	30
3.3	The angular <i>vs</i> momentum acceptance of the PDS. Different colors shows different STOP counters. With this distributions one can demonstrate that the telescopes are aligned along the focal plane.	31
3.4	Sketch of side view of the NDS, most of which are inside the D2 return yoke.	32
3.5	The angular <i>vs</i> momentum acceptance of the NDS. Different colors indicate different STOP counters.	34
3.6	Schematic top view of the forward scintillation hodoscope with the typical particle track.	35
3.7	The angular <i>vs</i> momentum acceptance of the FDS. Different colors indicate different STOP counters.	36
3.8	Common read out scheme for scintillator counters at ANKE .	38
4.1	ANKE Cartesian coordinate system.	42
4.2	Two geometrical cut conditions: Top view (a) for showing START–STOP combinations and front view (b) how to reject rescattered tracks from D2 poles.	43
4.3	Left: START–STOP combinations for the horizontal acceptance cut. Middle: YY–correlation for both chambers and its projection for the vertical acceptance cut at the right figure. .	44

4.4	Left: START–STOP combinations for the horizontal acceptance cut. Middle: YY–correlation for both chambers and its projection for the vertical acceptance cut at the right figure. .	45
4.5	Left histogram shows YY–correlation for the forward direction and the right figure is the target distribution in Y direction. .	46
4.6	Detection efficiency for K^+ and π^+ mesons. Also the ratio of K^+/π^+ detection is shown and interpolated over the whole momentum range.	47
4.7	The average detection efficiency over one run for different particles for each run is shown for the 3 beam times at 2.65, 2.70, and 2.83 GeV.	49
4.8	Sketch of electronics scheme to monitor the DAQ efficiency using experimental data. DAQ trigger is switched to "1" when the data writing is on.	52
4.9	The average DAQ efficiency for each run is shown for the 3 beam times at 2.65, 2.70, and 2.83 GeV. Deviations at the high energy are due to an unstable target thickness over time while at the other energies it has been stable.	53
4.10	Left: TOF between VETO and STOP counters is shown. Right: Normalized TOF over all START–STOP combination is shown.	54
4.11	Right: TDC value Vs. calculated time difference between NDS and PDS for one STOP-STOP combination using momentum information from $\pi^+\pi^-$ pair. Left: The sum of all normalized TOF difference of the PDS and NDS STOP counters are shown.	56

4.12	The left column shows: the TOF differences between the STOP counter in the negative as well as in the forward detector system with respect to the positive STOP counters versus TOF calculated using momentum information under the assumption that detected particles are K^+K^- and K^+ proton. The right column shows its projection where clear separation between this pair can be performed.	57
4.13	Missing mass of pK^+K^- at 18.5, 34.5 and 75.9 MeV excess energies.	59
4.14	Invariant mass of K^+K^- at 18.5, 34.5 and 75.9 MeV excess energies.	60
5.1	The SAID differential cross-section at three beam energies for proton-proton elastic scattering. Angular range from 4° to 10° degree is equivalent to detector acceptance.	62
5.2	Left: Efficiency corrected 2 dimensional histogram of event distribution over the polar and azimuthal angular range. Right: Efficiency map for the forward MWPCs used for luminosity determination.	63
5.3	Typical histograms to defined detector edges in azimuthal directions for $\Theta_{pol} = 5.25^\circ, 6.25^\circ, \text{ and } 7.25^\circ$	64
5.4	The proton missing mass spectra.	65
5.5	Efficiency corrected missing proton mass spectra for $\Theta_{pol} = 5.25^\circ, 6.25^\circ, \text{ and } 7.25^\circ$. Under the peak dashed area shows background.	66
5.6	Angular distribution at excess energy of 18.5 MeV. The fitting function is the differential cross-section for the same beam energy. There is one fitting parameter which is used to calculate the luminosity.	67

5.7	Angular distribution at excess energy of 18.5 MeV. The fitting function is the differential cross-section for the same beam energy. There is one fitting parameter which is used to calculate the luminosity.	68
5.8	Average frequency shift ($\frac{\Delta f}{\Delta t}$) of the center of gravity of the Schottky spectra over one cycle. Red lines shows where the cycle have been started and where it was finished.	71
5.9	Relative change of f_0 versus relative change of the dipole field.	72
5.10	The beam current measured at two different points of COSY ring. Solid line shows the BCT signal from device located close to ANKE experiment while dashed line is from device close to EDDA experiment.	73
5.11	Typical values for target thickness during one run.	74
5.12	Typical values for luminosity during one run.	75
5.13	Comparison of the luminosity determined by the Schottky method ▼ and by elastic scattering ▲.	75
6.1	Raw (l.h.s) and efficiency corrected (r.h.s) M_{inv}^{KK} distribution for 3 excess energies. The solid histogram shows the background contributions which have been estimated by the side band events in the missing mass distributions of the non-detected proton (described in the text). For the highest energy the misidentified background contribution is already subtracted in the corrected spectrum.	82
6.2	Total cross section for ϕ and ω -production in pp collisions as a function of excess energy. The error bars include both statistical and systematic uncertainties. Inset: the dashed line shows a phase space calculation normalized to pass through the highest energy ANKE point, while the solid line, which includes pp final state interaction effects, is a fit to all the ANKE data.	84

6.3	Differential distributions for $\varepsilon=18.5$ MeV. Vertical error bars indicate statistical uncertainties and horizontal ones bin widths. Upper left panel: $d\sigma/d\Omega$ as a function of the cosine of the polar K^+ in the reference frame of the ϕ -meson relative to the beam direction. The full line is the expected $\sin^2 \Theta_\phi^{K^+}$ shape. Lower panels: $d\sigma/d\Omega$ vs. cosine of the polar angle of the ϕ meson in the overall c.m. system (left), polar angle of the emitted proton (middle), and proton polar angle relative to the ϕ direction (right), the two latter being in the (pp) reference frame. Upper right: Dependence of the cross section on the pp relative momentum. The dotted line reflects pure phase space whereas the solid includes also the pp FSI.	86
6.4	Total ϕ - and ω -cross sections in pp collisions below 100 MeV excess energy. The solid line is a fit through the ω data points.	89
6.5	Total ϕ - and ω -production cross sections in pp collisions. The three lines show the energy dependence of three-body phase space including the effect of final-state-interaction (FSI) normalized to the ω (top) and ϕ (middle and bottom) cross sections. The middle line is normalized to the three low-energy ANKE points (stars), while the lowest line is fixed by the high energy ϕ cross sections.	90
6.6	New $pp \rightarrow pp\phi$ ANKE data at 75.9 MeV: lhs. shows the missing mass spectrum of the nondetected proton, and rhs. the corresponding K^+K^- invariant mass distribution.	92
B.1	The ratio between summarized PDS START counts and integrated luminosity derived via Schottky analysis (for Run 7247) is shown in Fig: B.2 with standard deviation less than 2%. . .	96
B.2	Ratio between integrated luminosity derived via pp -elastic scattering and sum of PDS START counts at $T_{beam} = 2.65, 2.70$ and 2.83 GeV.	97

Acknowledgments

I would like to thank Prof. Dr. H. Ströher for providing the possibility to do this work at his institute, for giving advice, for reading the thesis, and for useful comments.

I would like to thank Prof. Dr. M. Nioradze for the consent to act as the adviser of my thesis.

I wish to express my gratitude to Dr. M. Hartmann for useful discussions. I was really happy to get a chance to learn things in computing, which are not written in the text books.

I would like to express my deep respect to Dr. Y. Maeda who will be for me as an example of the hardest worker scientist forever.

I wish to thank to Dr. A. Kacharava who is permanently maintaining a friendly working environment.

The efforts of COSY staff are also acknowledged. I would also like to thank all the rest of the ANKE collaboration members. I could not have imaged having a better working atmosphere at the Institute.

I would like to say a big “thank-you” to all the people who agreed to be interviewed by me for this thesis. Especial thanks to Prof. C. Wilkin, Dr. H. J. Stein and others.

I also warmly thank my friends and colleagues in the Institute to keep me in shape.

Finally I would like to extend my deepest gratitude to my Family.